ADVANCED ENERGY MATERIALS
www.advenergymat.de

Advanced Characterization Techniques for Overcoming Challenges of Perovskite Solar Cell Materials

*Min-cheol Kim, So-Yeon Ham, Diyi Cheng, Thomas A. Wynn, Hyun Suk Jung, and Ying Shirley Meng**

In the last 10 years, organic–inorganic hybrid perovskite solar cells have achieved unprecedented advances, to the point where they now exhibit extremely high efficiency. However, long-term stability and areal scalability limitations impede the commercial application of perovskite materials, and appropriate diagnosistic tools have become necessary to evaluate perovskite materials. Characterization of perovskite materials is regularly misinterpretated, due to unique intrinsic and extrinsic factors: degradation from the measurement source, ion migration, phase transition, and separation. Herein, studies on perovskites are reviewed that have used advanced characterization tools to overcome characterization challenges. Cryogenic temperature assisted measurements mitigate degradation or phase transitions induced by the measurement source. In situ measurements can track the variation of perovskite materials depending on external stimuli. Spatial material properties are able to be evaluated by the use of multidimensional mapping techniques. An overview of these advanced characterization tools that can overcome the challenges associated with established tools provides the opportunity for further understanding perovskite materials and solving the remaining challenges on the road to commercialization.

1. Introduction

Harnessing renewable energy is unquestionably the solution to the world's soaring energy demands and the current global climate crisis. Solar energy is the most abundant renewable resource available in the Earth,[1] and is therefore extensively studied by researchers across the globe. Photovoltaics have drastically improved between 1st and 3rd generations, showing decreasing the cost of manufacturing while maintaining power efficiency.[2] More recently, high-efficiency and low-cost hybrid organic–inorganic halide perovskite materials have emerged as the most promising light absorber for the new generation of photovoltaics replacing commercially dominant polycrystalline silicon materials.[3–8] After demonstrating solid-state perovskite solar cells (PSCs) in 2012,[9] the volume of research for PSC has massively increased. Consequently, power conversion efficiency of PSCs has rapidly developed, currently exceeding 25%, surpassing Cu(In,Ga)Se_2 (CIGS) and cadmium telluride (CdTe), and approaching to single crystalline silicon solar cells.[10] Despite the promising high power efficiency, PSCs are still far from commercialization due to their low stability and less scalability.[11,12] Together with improving efficiency of PSCs, researchers have been trying to enhance the device stability and develop large-area compatible fabrication method.[13,14] In spite of these effort, the state-of-the-art PSCs only retain performance for a few thousand hours under accelerated testing conditions, equivalent to a year or less of typical operation,[15–17] while 20 years of stability is required as a minimum for commercialization. At the same time, PSC modules are relatively low area (800–6500 cm^2) while only exhibiting 16% of power conversion efficiency (PCE) while commercialized silicon solar cells achieve over 22% of PCE with large module sizes (>14 000 cm^2).[18] To secure long-term stability and scalability, accurate characterization of perovskite materials is needed.

To understand root causes of the high efficiency, degradation mechanisms and low scalability of perovskite materials, the absorbing layer and devices have been extensively characterized.[19–22] Characterization tools commonly utilized for evaluating chemical, morphological, structural, optoelectronic properties of perovskite are summarized in **Figure 1**, and their resolution limit is summarized in **Table 1**. In the scope of chemistry, the electronic band structure and chemical composition of perovskite material have been elucidated with various spectroscopies and measurements using UV-visible spectroscopy (UV–vis), ultraviolet photoelectron spectroscopy (UPS), Kelvin probe forced microscopy (KPFM), X-ray photoelectron

Dr. M.-c. Kim, Dr. T. A. Wynn, Prof. Y. S. Meng
Department of NanoEngineering
University of California San Diego
9500 Gilman Drive, La Jolla, San Diego, CA 92093, USA
E-mail: shmeng@ucsd.edu
S.-Y. Ham, D. Cheng, Prof. Y. S. Meng
Materials Science and Engineering Program
University of California San Diego
9500 Gilman Drive, La Jolla, San Diego, CA 92093, USA
Prof. H. S. Jung
School of Advanced Materials Science and Engineering
Sunkyunkwan University
2066, Seobu-Ro, Jangan-gu, Suwon, Gyeonggi-do 16419, Republic of Korea
The ORCID identification number(s) for the author(s) of this article can be found under https://doi.org/10.1002/aenm.202001753.

DOI: 10.1002/aenm.202001753

© 2020 WILEY-VCH Verlag GmbH & Co. KGaA, Weinheim

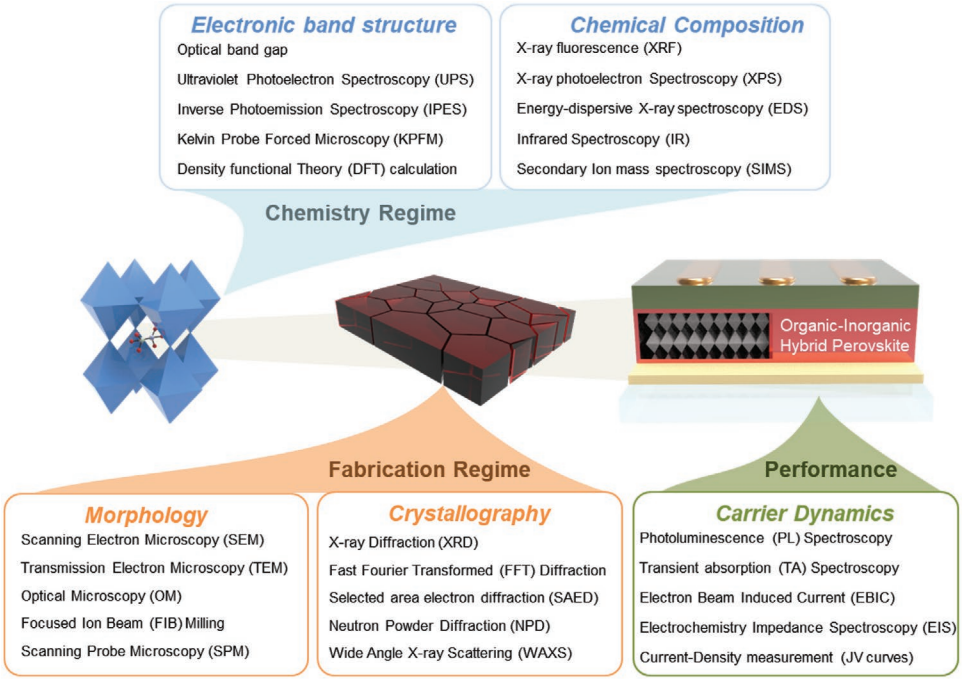

Figure 1. Summary of characterization tools utilized in the perovskite solar cell research field.

spectroscopy (XPS), and X-ray fluorescence (XRF).[23–27] Morphological and crystallographic characterization approaches, including electron microscopies (EM), X-ray diffraction (XRD) and atomic force microscopy (AFM), are also applied, especially useful for characterizing fabrication method development and validating the quality of perovskite thin films.[28–30] Synchrotron techniques such as extended X-ray absorption fine structure (EXAFS) or X-ray absorption near edge structure (XANES) have also been recently adopted to evaluate perovskite materials, providing deeper chemical, structural information than the result from the conventional laboratory X-ray sources.[31] A. Sharenko et al. reported the lead coordination of $MAPbI_3$ precursor as a function of precursor solution chemistry (PbI_2, MAI, HI) from the Pb L-III edge EXAFS and XANES measurements. Synchrotron X-ray sources enable X-ray absorption measurement since they have higher X-ray flux, broader spectral range, and higher stability of beam irradiation. Neutron diffraction study was also conducted for perovskite materials to investigate the crystal structure.[32] In the study of Yang et al., in situ neutron diffraction measurement for $MAPbBr_3$ as a function of temperature revealed that transition of MA^+ cations to disordered arrangement induced phase transition from orthorhombic to tetragonal. Neutron diffraction is similar to X-ray diffraction but since neutrons scattered from nuclei of the atoms while X-ray scattered from electrons, neutron diffraction can discriminate the ordering of organic cations in perovskite materials. Carrier dynamics such as generation, transportation and recombination of charge carriers are probed and evaluated by characterization tools after fabrication as full photovoltaic devices.[33,34] However, these conventional characterization methods are mostly adopted from other fields such as dye sensitized and thin film solar cells or conventional oxide and fluoride perovskites, and consequently have not been optimized for halide perovskite materials research. Since organic–inorganic hybrid perovskite materials contain organic cations and exhibit environmental instability, charge accumulation and ionic migration during device operation, these conventional methods cannot be easily implemented for PSCs. Considering that X-ray, laser, and

Table 1. Summary of the spatial and other resolution limits for each characterization tools used to evaluate the properties of perovskite materials.

Measurement	Spatial resolution limit		Other resolution limit (energy or temporal)
	Lateral	Vertical	
XPS	5 µm to 5 mm	2–10 nm	Energy: 0.5–1 eV
UPS	5 µm to 5 mm	2–3 nm	Energy: 0.01–0.02 eV
Raman	1 µm	Few µm to mm	Energy: a few cm^{-1}
AFM	0.1–5 nm	<0.03–0.1 nm	N/A[a)]
KPFM	10–50 nm	<0.03–0.1 nm	Energy: <10 mV
XRF	10–150 µm	10 µm	Energy: 3 – 150 eV
EDS	Bulk 1 µm	0.02–1 µm	Energy: 40 – 150 eV
	Thin 1 nm		
IR	20 µm to 5 mm	10 nm to a few µm	Energy: a few cm^{-1}
SIMS	10 nm to 2 µm	0.3–2 nm	N/A
SEM	1–100 nm	A few nm to a few µm	N/A
TEM	0.2 to 5 nm	None	N/A
XRD	≈10 µm (microfocus)	A few µm	Energy: 150 – 500 eV
PL	1–2 µm	0.1–3 µm	Temporal: few ps – ns
TA	50 nm A few µm	None	Temporal: 500 fs

[a)]Not applicable.

© 2020 WILEY-VCH Verlag GmbH & Co. KGaA, Weinheim

Table 2. Characterization techniques and common artifacts reported.

Characterization	Source	Artifacts	Ref.
XPS	X-ray	Advent of Pb(0) XPS peak	[37]
XRD	X-ray	Crystal phase intensity decrease	[60]
Transient absorption	Laser	Transient reflection interference	[189]
Raman	Laser	PbI_2 and PbO generation from degradation	[190]
UV–vis	Lamp	Light scattering and red shift	[191]
FIB	Ion beam	Optical loss from degradation	[192]
ToF-SIMS	Ion beam	Degradation, implantation and bond breaking from the primary ion	[193,194]
SEM	Electron beam	Degradation of Pb^{2+} into Pb^0, electron beam induced ion migration, C-N bond breakage for organic cation	[35,36,195,196]
EBIC	Electron beam	Electron beam induced current decrease as time	[35]
TEM	Electron beam	Degradation of Pb^{2+} into Pb^0	[197]
JV	Electrical bias	Current voltage hysteresis and electric field induced degradation	[40,198]

electron beam sources may accelerate the degradation of perovskite materials by localized temperature increase, there can be severe artifact generation during the characterization.[35–38] PSCs also suffer from current–voltage hysteresis behavior or phase separation problem due to ion migration and charge accumulation while operation under light illumination.[39–42] Some of the common artifacts reported during characterization for perovskite materials are summarized in **Table 2**. Therefore, conventional characterization methods require optimization to be suitable for PSC research.

Herein we have reviewed some characterization challenges for PSCs due to their unique intrinsic and extrinsic properties such as fast degradation, phase transition, and ion migration. More importantly, we showcase some of the recent advanced characterization techniques developed for perovskite materials which are modified from conventional characterization tools to suppress ion mobility, minimize beam damage, track the variation of the devices, and map the spatial distribution of material properties.

2. Characterization Challenges for PSCs

Advancing PSCs by achieving higher PCEs, changing perovskite absorber chemistry and transport materials for improved stability, or developing lead-free perovskite materials, requires the aid of appropriate characterization techniques. However, most of the characterization tools as mentioned before for current PSC research are adopted from alternate solar cell or oxide-perovskite material fields. Characterization methods established in other fields enable PSC materials to experience extremely rapid development, though without modification, they may also lead to misinterpretation when applied to PSC materials. Organic–inorganic halide perovskite materials have their own unique properties such as photoinduced degradation, giant dielectric constants, phase transitions or separation, and current–voltage hysteresis effects as described in **Figure 2**.[39,43–45] Organic cations and halide anions are observed to migrate in perovskite materials that accelerates the degradation, phase transition and induce polarization or hysteresis effects.[42,46,47] These unique properties require modifications or combination with other techniques to mitigate abnormal effects observed in perovskite materials. In this section, we address the challenges originated from the unique properties of perovskite materials that cause difficulties for characterizing.

2.1. Perovskite Decomposition Due to Source Beam Damage

As we discussed above, organic–inorganic halide perovskite materials have several unique properties that impede proper interpretation of characterization results due to artifacts from the measurements. Foremost, perovskite materials are vulnerable to the contents of ambient air, including oxygen and moisture, while under the light illumination. Perovskite materials absorb water very easily,[48] forming a perovskite hydrate compound which is fairly reversible. Light exposure to perovskite materials can break weak bonds within the perovskite,[38,43,49] generating ion defect vacancies which enable ions and vacancies to migrate. Perovskite materials have fragile crystal structure susceptible to parasitic vacancies (defect sites), and degradation may be further accelerated by electric fields induced from ion migration.[11,47,50] Moreover, photoillumination also converts oxygen to highly reactive superoxide which reacts with perovskite materials, leading to the decomposition into lead iodide (PbI_2) or other byproducts.[43,51]

Perovskite materials are also prone to degradation by thermal energies. Methylammonium lead iodide ($CH_3NH_3PbI_3$), which is the most common perovskite materials for solar application, can decompose into various kind of by-products such as 1) methylamine (CH_3NH_2) gas and hydroiodic acid (HI)[52] 2) methyl iodide (CH_3I), and ammonia (NH_3) gases.[53] Formamidinium lead iodide ($CH(NH_2)_2PbI_3$) which is known to have relatively higher thermal stability also decomposes into hydrogen cyanide (HCN), NH_3, HI and PbI_2 at high temperature.[54] All the degradation routes and byproducts are described in **Figure 3**a. Due to photolysis and pyrolysis, perovskite materials are decomposed into gaseous byproducts, PbI_2, and metallic lead which are the most common artifacts.

Meanwhile, most of the characterization tools inevitably require specific sources or environments to operate. Characterization sources including X-rays,[55,56] ultraviolet radiation,[57] pulsed lasers with various wavelengths,[58] electron beams,[29] and electrical bias[59] can easily generate localized thermal vibration or function as light illumination when interacting with perovskite materials. As mentioned before, the degradation of perovskite materials under light illumination and thermal stress are critical problems during the characterization using these sources. Beam radiation damage from X-ray, ultraviolet, electron beam makes it difficult to interpret the measurement results properly since they introduce artifacts in the spectra, reflections or images. For instance, Hoye et al. reported beam damage from X-rays while performing

© 2020 WILEY-VCH Verlag GmbH & Co. KGaA, Weinheim

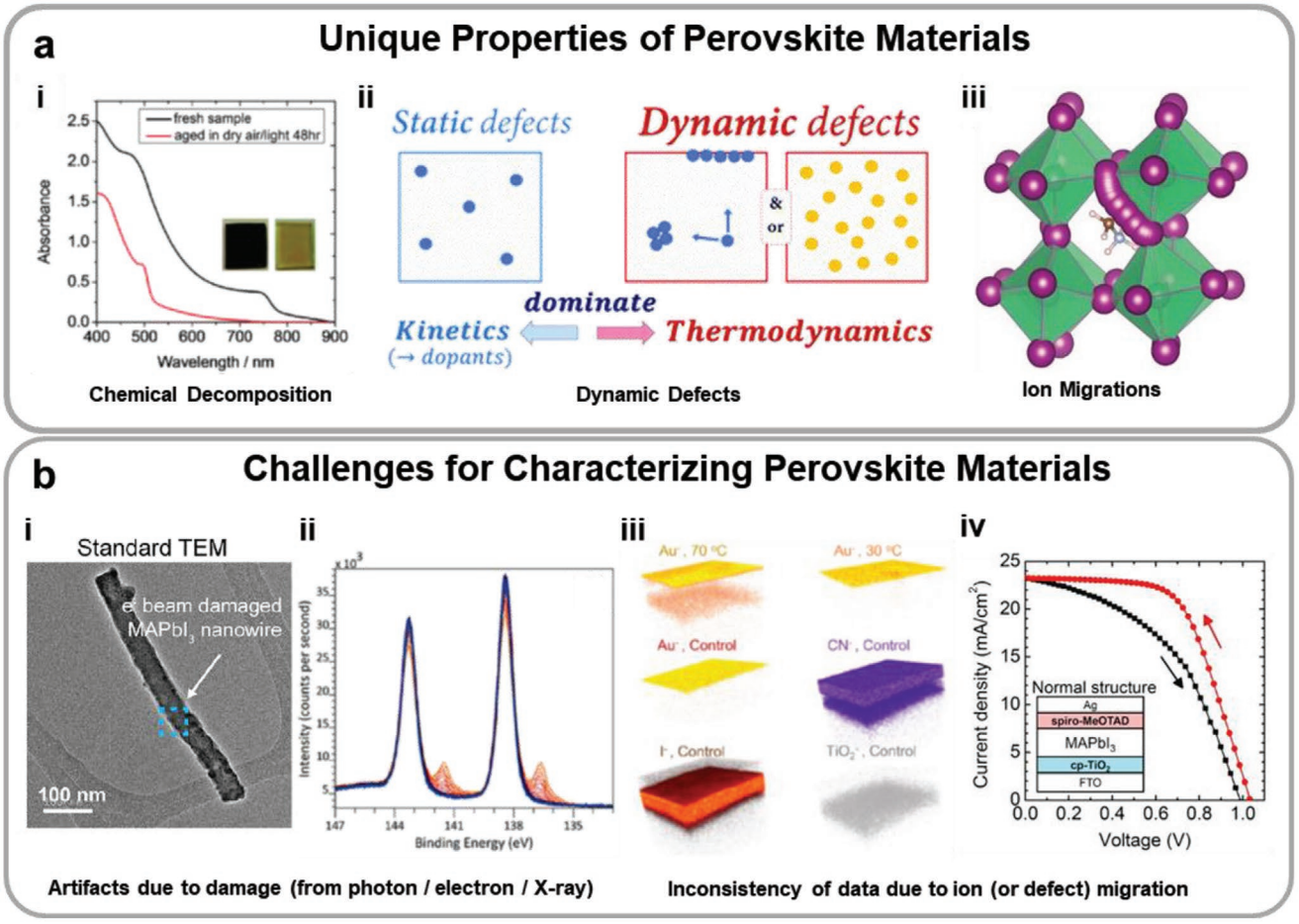

Figure 2. a) Unique properties of organic–inorganic hybrid perovskite materials that impede robust characterization of perovskite materials. i) Reproduced with permission.[38] Copyright 2016, Royal Society of Chemistry. ii) Reproduced with permission.[199] Copyright 2019, Royal Society of Chemistry. iii) Reproduced with permission.[47] Copyright 2015, Springer Nature. b) Examples of artifacts due to damage from photon, electron and X-ray beam and inconsistent measurement results of PVSK materials due to ion migration. i) Reproduced with permission.[104] Copyright 2019, Elsevier. ii) Reproduced with permission.[37] Copyright 2019, Elsevier. iii) Reproduced with permission.[182] Copyright 2016, American Chemical Society. iv) Reproduced with permission.[39] Copyright 2015, American Chemical Society.

continuous XRD measurement for an hour in air ambient as depicted in Figure 3c.[60] McGettrick et al. also reported X-ray induced damage with the advent of Pb^0 artifacts during XPS analysis of lead halide perovskites as shown in Figure 3d.[37] They revealed that the evolution of Pb^0 occurs via X-ray photolysis under typical analytical conditions. Likewise, Xiao et al. and Liu et al. studied the electron beam induced degradation of perovskite materials that is inevitable in scanning and transmission electron microscopy (SEM and TEM) observation, claiming that the defect formation by irradiation damage and the intermediate phase formation induced by electron beam heating are observed (Figure 3e).[36,61] Significant beam damage can occur when measuring the perovskite materials, no matter the source, if it has sufficient energy. Therefore, it is essential to evaluate and exclude the damage by radiation of the probe on the system so to properly interpret the data.

As the light- and heat-induced degradation of perovskite materials are highly dependent on the atmospheric conditions, it is also important to understand what conditions can be taken to minimize the effects of radiation damage during the characterization. The best way of mitigating the damage is to consider atmosphere of the measurement. For example, filling the measurement chamber with the inert gases like N_2, Ar, He can minimize the extent of perovskite damage effectively.[60] Considering that the light intensity and temperature is critical for the degradation of perovskite materials, finding the minimum source power to acquire the desired signal from the sample is also important to minimize the artifacts in the data. However, in this case, despite all the efforts to minimize the beam damage from the source, it is impossible to rule out beam damages and eliminate artifacts from the results completely. It will be discussed later how researchers modify measurements for perovskite materials to minimize beam damage.

2.2. Phase Transition and Separation

Besides the photolysis and pyrolysis processes for perovskite materials, crystal phase transitions are also a source of inconsistency during characterization. In the typical solar operating

© 2020 WILEY-VCH Verlag GmbH & Co. KGaA, Weinheim

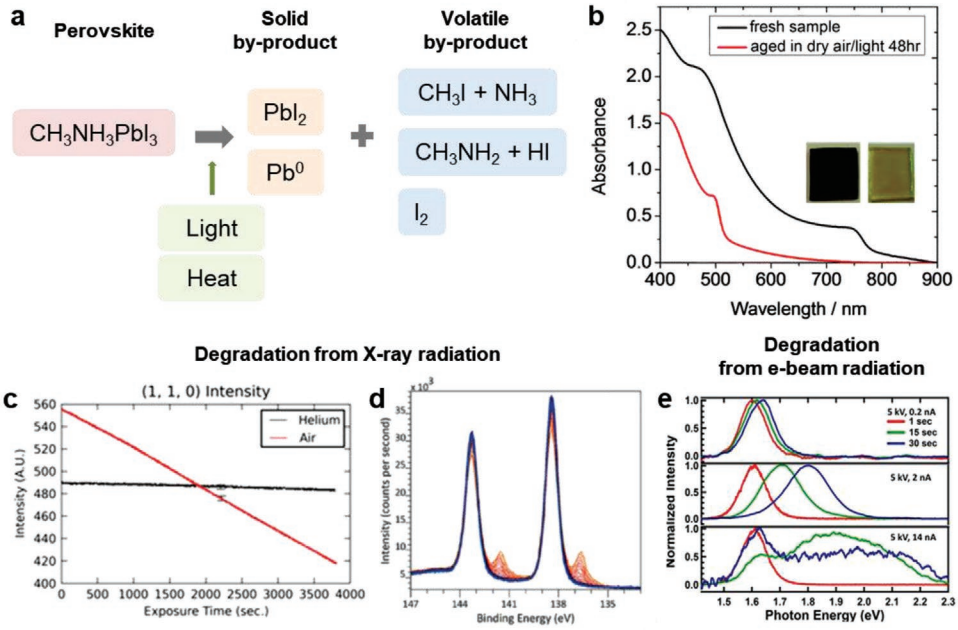

Figure 3. a) Photo- and temperature-induced decomposition routes for perovskite materials ($MAPbI_3$), leading to three different processing routes including reversible (CH_3NH_2 + HI and I_2 + Pb^0) and irreversible volatile byproducts (CH_3I + NH_3). b) Absorption spectra of fresh and degraded perovskite ($MAPbI_3$) films and their photo. Reproduced with permission.[38] Copyright 2016, Royal Society of Chemistry. c) Time-evolutional decrease of XRD intensity of (110) peak of perovskite ($MAPbI_3$) film with continuous X-ray radiation. Reproduced with permission.[60] Copyright 2017, American Chemical Society. d) A gradual time-evolutional generation of Pb(0) XPS peak with continuous X-ray radiation in perovskite ($MAPbI_3$) film. Reproduced with permission.[37] Copyright 2019, Elsevier. e) Change of peak position and intensity for CL measurement of perovskite ($MAPbI_3$) film with time under continuous electron beam illumination. Reproduced with permission.[36] Copyright 2015, American Chemical Society

temperature range (25–85 °C), there are two main phase transitions for common perovskite materials ($MAPbI_3$ and $FAPbI_3$) used as solar application: the first one is tetragonal to cubic phase transition for $MAPbI_3$ based materials and the second is cubic (α–) phase to hexagonal (δ–) phase transition for $FAPbI_3$ based ones.[45,62,63] Generally, structural stability of ABX_3 perovskite materials can be determined by the Goldschmidt tolerance factor (t)

$$t = \frac{r_A + r_X}{\sqrt{2}(r_B + r_X)} \quad (1)$$

where r_A, r_B, r_X are the radius of the A cation, the B cation, and the X anion, respectively; perovskite structures are formed when t is between 0.71 and 1.[64] Formamidinium (FA) based perovskite materials are more suitable for high efficiency solar cell applications with a lower bandgap and thereby wider light-absorbing window,[65,66] but conversely, the Goldschmidt tolerance factor suggests that FA cations are too large for the perovskite structure as depicted in **Figure 4**a. Given that the tolerance factor of pure-FA perovskite is over 1, it is easy to form the non-photoactive, yellow δ-phase at room temperature (Figure 4b), while pure-MA perovskite with a tolerance factor of 0.91 maintains the black, photoactive perovskite structure at operating temperature as well as at room temperature. Researchers have successfully achieved black α-phase perovskite $FAPbI_3$ perovskites by modifying the fabrication procedure, but the α-phase is metastable which reverts to the yellow δ-phase within several hours or days.[67–70] Even with a lower phase stability of $FAPbI_3$, FA perovskites are more resistant to thermal decomposition and photolysis than MA perovskites, therefore stabilization of FA based perovskites is needed.[65]

Possible origins of phase transition for perovskites are reported to be temperature, moisture, light, or pressure.[45,71–74] For FA based perovskite materials, at temperatures below the transition (130 °C), FA^+ cation groups aligned with strong preferential orientations apply strains to the α-phase cubic crystal toward specific direction which distorts and drives the structure to the δ-phase. With the existence of moisture at ambient conditions, this process can be greatly accelerated because highly hygroscopic FA^+ cations react with moisture and cause instability of α-phase cubic crystal as shown in Figure 4c.[65,71,75] Researchers also reported that $FAPbI_3$ undergoes a pressure-induced phase transformation and amorphization of the perovskite due to the lattice shrinkage from the volume compression as shown in Figure 4d,e.[74,76] Ultrahigh vacuum conditions were also observed to induce phase transitions in perovskite materials through lattice and crystal volume expansion, accompanying structural instability.[77] Many characterization tools need pressure control, mostly at the high vacuum level, in order to reduce artifacts from forming even before measurements are taken.

2.3. Ion Migration and Charge Accumulation

Inorganic perovskite oxides have been observed to exhibit high ionic conductivity mediated by defect species.[78,79] Some inorganic perovskite halide research suggests that halide

© 2020 WILEY-VCH Verlag GmbH & Co. KGaA, Weinheim

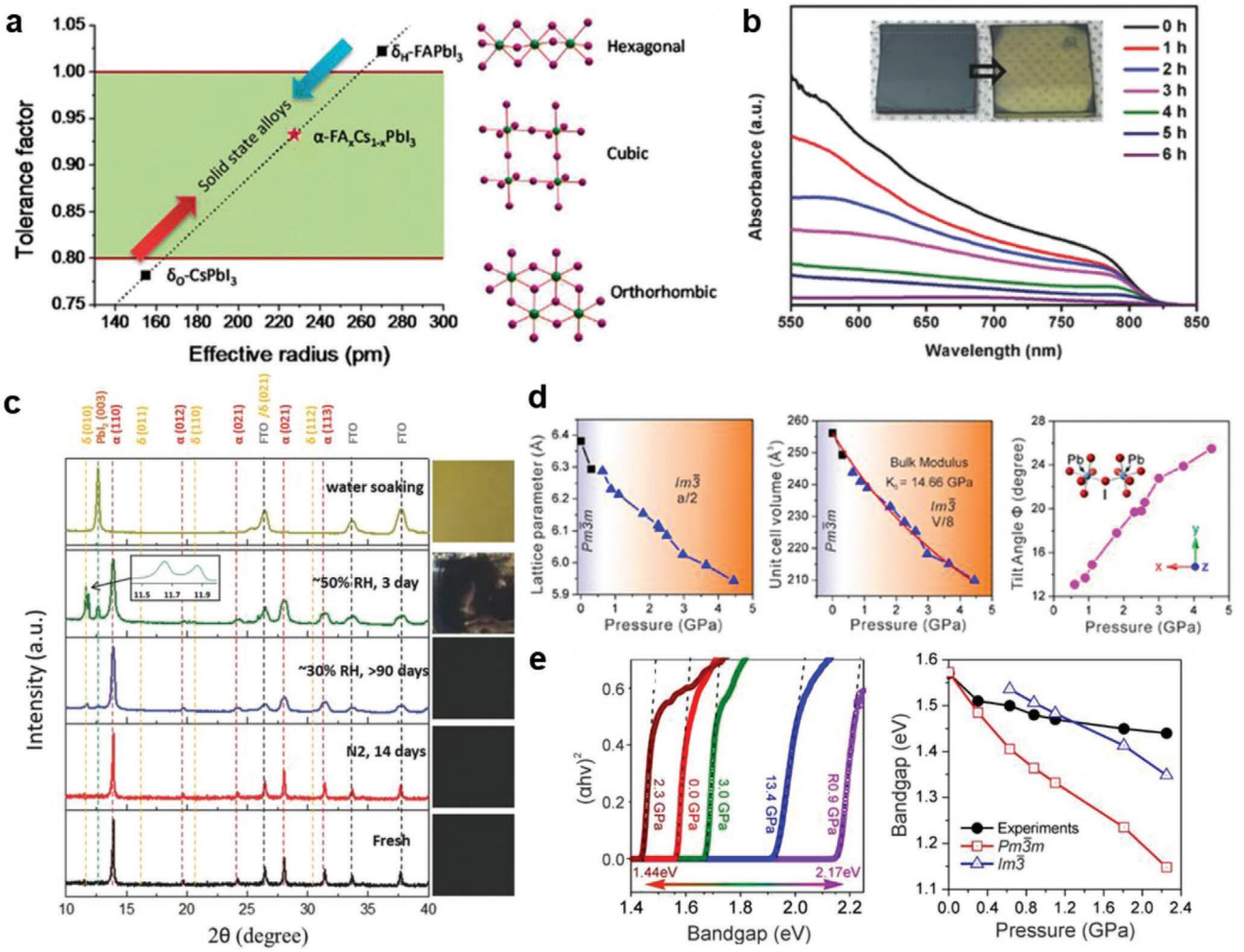

Figure 4. a) Tolerance factor diagram for perovskite materials. Reproduced with permission.[88] Copyright 2016, American Chemical Society. b) Phase transition from black α-phase to yellowish δ-phase of FA based PSCs. Reproduced with permission.[200] Copyright 2017, Wiley. c) Moisture-induced phase transition of FA based perovskite materials. Reproduced with permission.[71] Copyright 2018, Wiley. d) Pressure-induced phase transition of perovskite ($FAPbI_3$) materials and e) corresponding band-gap transition induced by phase transition. Reproduced with permission.[74] Copyright 2018, American Chemical Society.

ions have even lower activation energies for migration than oxygen.[80,81] Likewise, in the organic–inorganic halide perovskite materials utilized in PSCs, charged defect sites from the vacancies of compositing ions can be easily formed and are highly mobile because they have relatively low defect formation energy.[82,83] Consequently, compositing ions, especially the organics cations (MA^+, FA^+) and halide ions (I^-, Br^-), can easily migrate via ion vacancies along the perovskite films as shown in **Figure 5**a.[47] Formation of the vacancies or defects and ion migrations provoke charge and ion accumulation at the defect sites or interfaces between perovskite and transporting layers.[42] Halide perovskite materials are known to have defect tolerance that enables them to maintain their performance even after the formation of defect sites, which is different from the Silicon-based solar cells.[84] Though halide perovskite materials are relatively free from carrier loss via trap assisted recombination owing to the defect tolerance, ion migration (Figure 5a) and accompanied ion/charge accumulation (Figure 5g) from defect sites are contemplated as the origin of intrinsic abnormalities such as the current–voltage (*I–V*) hysteresis, accelerated degradation, and phase separation which make characterization difficult.

Ion migration has a vast impact on electrical evaluation methods such as *I–V*, electrochemical impedance spectroscopy (EIS), and regarding photovoltage or photocurrent measurement. This is because PSCs are mutiphysical system with combined electron flux and ion flux. The *I–V* hysteresis issue has been a pervasive issue in perovskite materials (Figure 5h),[39] and researchers are developing proper measurement protocols with the consideration of hysteresis behaviors. Phase separation issue originated from ion-mixing strategies for perovskites at A-site, B-site, or X-site to stabilize FA based perovskites.[85–87] Incorporation of inorganic cations (Rb, Cs) or different organic cations (MA) at A-sites with specific portions of Br at the X-site can help to stabilize α-phase $FAPbI_3$ to match the tolerance factor as explained above.[88–90] Unfortunately, due to mobile ions such as halide ions and organic cations inside perovskite materials, many

© 2020 WILEY-VCH Verlag GmbH & Co. KGaA, Weinheim

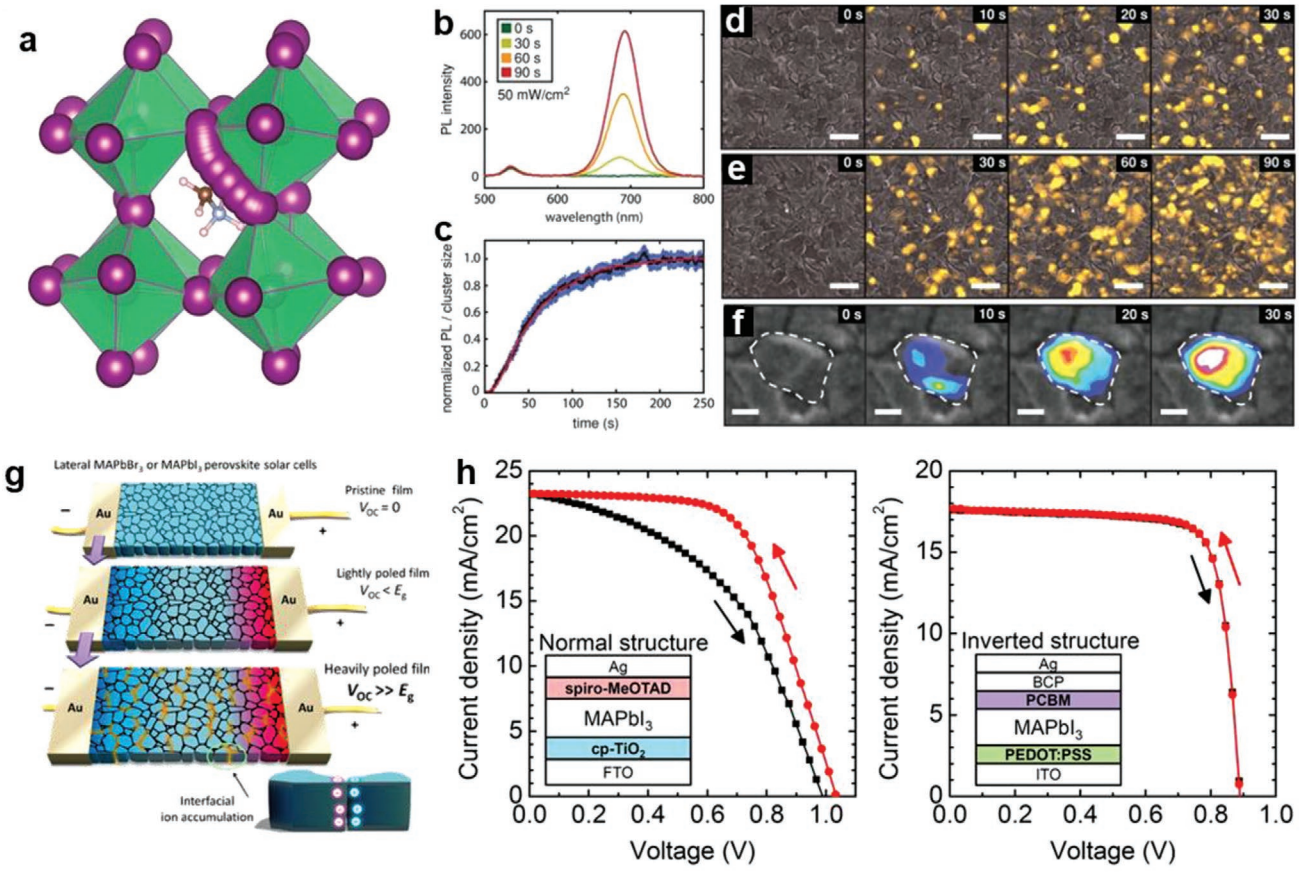

Figure 5. a) Schematic for halide ion migration inside the perovskite crystal. Reproduced with permission.[47] Copyright 2015, Springer Nature. b) Phase separation investigated by PL spectra after different light soaking times at 50 mW cm^{-2} and c) normalized PL intensity as time. CL image series with d) 10 and e) 30 s of light soaking between each CL image. The scale bars are 2 µm. f) CL image series of a single domain with 10 s between each image with the color indication of iodide-rich domain. The scale bar is 200 nm. $MAPb(I_{0.1}Br_{0.9})_3$ chemistry was used here for perovskite materials. Reproduced with permission.[91] Copyright 2017, American Chemical Society. g) Schematic for charge and ion accumulation at the interface of lateral perovskite device. Reproduced with permission.[201] Copyright 2017, The American Association for the Advancement of Science. h) Perovskite ($MAPbI_3$) devices with (left) and without (right) the current–voltage hysteresis. Reproduced with permission.[39] Copyright 2015, American Chemical Society.

studies on photoinduced phase separation were reported in mixed halide perovskite materials after acquiring phase stability of FA based perovskite materials by mixing halide ions.[91–94] Phase separation is accelerated with continuous photoillumination or electrical bias application and is observed with various of characterization tools. For example, as shown in Figure 5b–f, with continuous light illumination, iodide-rich clusters evolve over time which can be resolved with the evolution of luminescence intensity along the surface of perovskite layer.[91] In this way, artifacts from phase separation impede the proper interpretation of electronic, chemical, and optical properties of perovskite materials during the measurement.

3. Suppressing Ion Migration and Damage: Cryogenic Techniques

As discussed in the previous chapter, perovskite materials have been reported to decompose or undergo phase transformations easily upon exposure to ambient conditions when coupled with thermal or electromagnetic irradiation. However, much of our understanding of such degradation mechanisms are limited to the bulk state, and the nanoscale and atomistic perspective of the crystal structure, morphology, and physical properties of halide perovskite materials are still elusive. Most characterization tools used for evaluating the atomistic and nanoscale property of perovskite materials are limited to those using energetic probes such as X-ray/neutron diffraction, electron microscopy and surface-sensitive techniques such as XPS or time-of-flight secondary ion mass spectroscopy (ToF-SIMS). TEM has been applied to study the morphology of PSCs. While the atomistic understanding of perovskite crystal may provide the clue of degradation mechanism or performance enhancement, atomistic resolution imaging remains challenging due to the vulnerability of perovskite materials to beam irradiation.[95] It also remains difficult to prepare pristine samples to obtain intrinsic information without any artifacts from damage when using characterization tools with irradiation source. Minimizing the irradiation induced damage from the electron beam exceeding the critical electron doses is necessary to image sensitive materials without any artifacts.[96] Electron radiation can cause defect formation in perovskite materials (primary damage) and

© 2020 WILEY-VCH Verlag GmbH & Co. KGaA, Weinheim

produce localized electron beam heating leading to the degradation of perovskite materials (secondary damage).[36,97]

One of the easiest and simplest ways to mitigate the damage of materials from the electron beam irradiation is lowering the beam dose on the sample. By imaging at ultralow electron dose (11 e^{-} $Å^{-2}$), a high-resolution TEM images of a methylammonium lead bromide perovskite ($MAPbBr_3$) was successfully acquired.[98] However, this imaging condition cannot be applied for observing iodide based methylammonium lead iodide ($MAPbI_3$) without sample changes because thermal durability of $MAPbBr_3$ is higher than $MAPbI_3$. Cooling down the sample during the measurement is another approach to minimize the damage of perovskite material which comes from the irradiation of measurement sources. Inspired by the biological community, who originally developed cryogenic electron microscopy (cryo-EM) to visualize highly sensitive biological macromolecules,[99] cryo-EM has achieved great success in various material research fields,[100] including polymers, battery materials, nanoparticles, and even for metal halide perovskite materials.[101–104] Here is the summary of instrumental details to evaluate the electron beam-induced damage on perovskite materials during TEM and SEM observation in **Table 3**. Though cryo-EM has been utilized in perovskite materials to investigate crystal structure or nanoscale morphology with minimizing the beam-related damages to some extent, there is the opinion that cryotemperature induces undesired amorphization of the perovskite materials during the cryo-EM observation.[114]

3.1. Sample Preparation and Operation of Cryo-EM

Cryo-EM has been vigorously applied in materials research, especially in the Li-ion battery field. Cryo-EM related Li-ion battery research has focused on components such as anode materials (i.e., Li metal, Si and charged graphite), certain solid electrolytes (i.e., lithium phosphorus oxynitride and sulfides), charged cathodes and solid/cathode electrolyte interphases (S/CEI), which are all susceptible to both ambient atmosphere and beam irradiation.[105] The application of cryo-EM in the Li-ion battery field has enabled drastic progress in the characterization and development of next generation high energy materials for batteries. Perovskite materials are also composed of beam-sensitive organic cations and halide ions, thereby cryo-EM is one of the promising tools to preserve perovskites while exploring their atomic structure. Fortunately, sample preparation and processing procedures for cryo-EM can be adopted from the aforementioned materials.[102,106,107] A safe and robust sample preparation procedure for cryo-EM is demonstrated in **Figure 6**a,b. Particles prepared on a TEM grid by dispersion or thin lamella mounted onto the grid by cryofocused ion beam (FIB) can be used as a pristine sample. A FIB permits mounting of a target particle or region of interest from a film on the grid with the ability to control the thickness by milling. However, FIB milling is performed with high energy ions (typically Ga ions), frequently inducing sample damage due to local heating, ion radiation, and Ga implantation.[108] For perovskite materials, degradation of organic materials through decomposition from local heating and ion flux should be considered in order to minimize ion-milling-induced damage. One of the approaches used to mitigate damage during FIB preparation is milling samples under cryogenic temperature (typically around 100 K), which proved to be necessary for perovskite sample preparation.[109] The actual application of cryo-FIB on the perovskite materials will be discussed later in this chapter. After the samples are prepared on the grid, there are two kinds of commercially available holders developed for cryoTEM to load the grid and transfer the sample into the column. The first one is the cryotransfer holder (Figure 6a) and the other is the cooling holder (Figure 6b). The former can maintain the sample at liquid nitrogen temperature before and during loading into the TEM column, while the latter can protect the sample under the vacuum or an Ar-filled glovebag without any air exposure during transfer and then be cooled down with liquid nitrogen after

Table 3. Summary of instrumental details for the electron beam induced damage on perovskite materials.

Characterization tools	Accelerating voltag [kV]	Perovskite chemistry	Critical dose or maximum dose	Evaluation	Ref.
Cryo-TEM	200	$MAPbI_3$	12 e $Å^{-2}$	<2 Å diffraction intensity decay (30%)	[104]
Cryo-TEM	200	$MAPbBr_3$	46 e $Å^{-2}$	<2 Å diffraction intensity decay (30%)	[104]
Cryo-TEM	300	$MAPbI_3$	150 e $Å^{-2}$	Amorphization	[114]
Cryo-TEM	300	$MAPbBr_3$	81 e $Å^{-2}$	Amorphization	[114]
HRTEM	80, 300	$MAPbI_3$	13–16 e $Å^{-2}$ (at 80 kV) 38–39 e $Å^{-2}$ (at 300 kV)	Appearance of $MAPbI_{2.5}$ diffraction spot	[114]
HRTEM	300	$MAPbBr_3$	11 e $Å^{-2}$ (Not damaged)	Comparing with the simulated potential map	[98]
HRTEM	200	$CsPbCl_3$	Not provided (irradiated for 30 min)	Comparing SAED pattern	[61]
STEM	80, 200	$CsPbBr_3$	170 nanoclusters at 500 e $Å^{-2}$	Atomic ratio change from EDS, advent of metallic Pb^0	[197]
SEM	2, 5, 8, 10	$MAPbI_3$, $FAPbI_3$, $CsPbI_3$	2 nA for 15 s ($MAPbI_3$) 12 nA for 15 s ($FAPbI_3$)	Cathodoluminescence shift and intensity change	[36]
SEM	3	$MAPbBr_3$	5 pA for 60 µs	Morphological change	[35]
SEM	10	$MAPbI_3$	86 pA for 22 s	Morphology, photoluminescence, cathodoluminescence change	[195]
Low-energy SEM	4.5–60 V	$MAPbI_3$	10^{17} e cm^{-2} (60 V)	C—N bond breakage in XPS	[196]

© 2020 WILEY-VCH Verlag GmbH & Co. KGaA, Weinheim

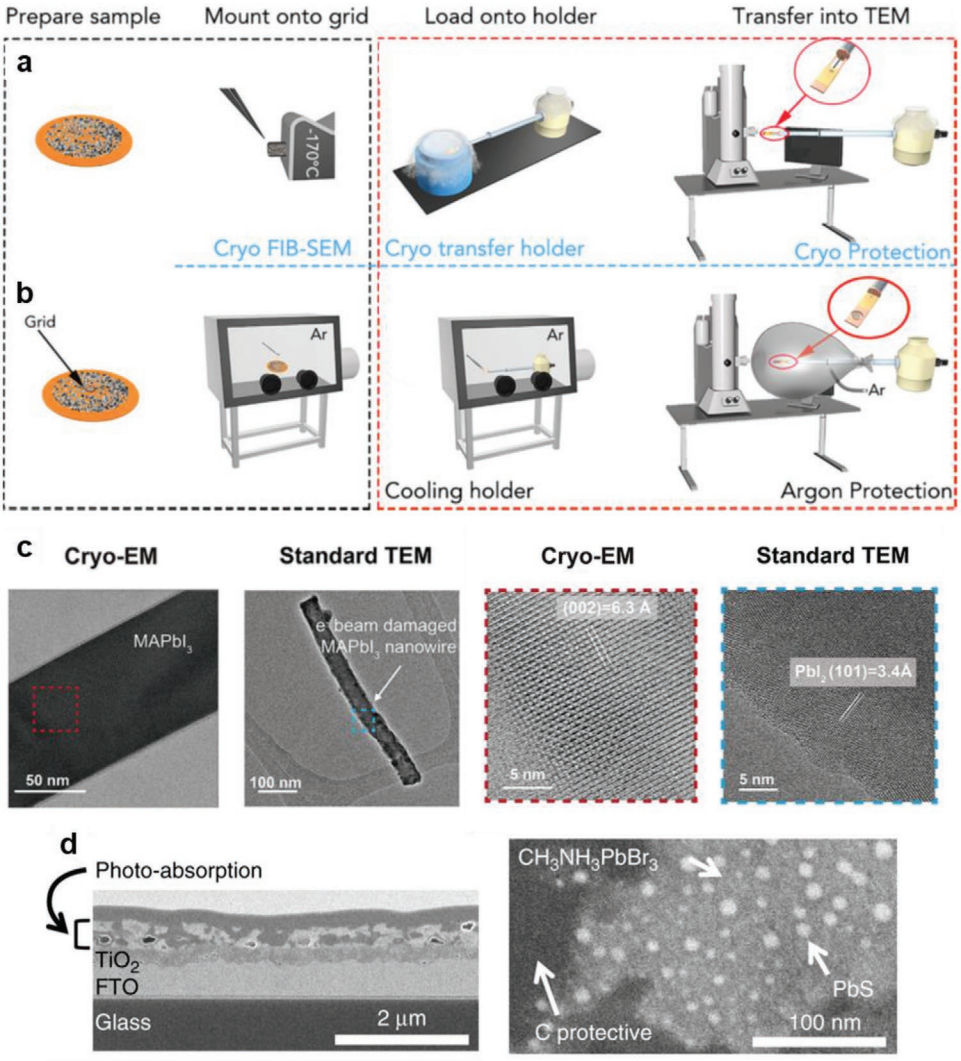

Figure 6. a,b) General schematics of procedure for Cryo-FIB and Cryo-TEM sample preparation. Reproduced with permission.[102] Copyright 2018, Elsevier. c) Transmission electron microscopy images with atomic resolution of $MAPbI_3$ nanowires prepared under cryotemperature and room temperature. Reproduced with permission.[104] Copyright 2019, Elsevier. d) Cryo-FIB and cryo-SEM images for PbS/$MAPbBr_3$ mixed composites performed at 153 K for analyzing with less perturbation of electron beams. Reproduced with permission.[112] Copyright 2019, Springer Nature.

inserting the holder into the TEM column. The cooling holder method is easier to operate than cryotransfer holder method, but the sample needs to be manipulated a under constantly inert environment, either under vacuum or with an inert gas filled system. In order to ease the procedure of cryo-EM observation, advanced cryoholders with self-sealing and faster cooling will be needed from the TEM holder developer. As cryo-EM is an emerging tool in the materials research field, in this chapter, we will discuss some pioneering research works in PSCs using cryo-EM characterization tools to mitigate the damage of electron and ion beam radiation during EM observation.

3.2. Application of Cryo-EM on Perovskite Materials

To fully elucidate atomic scale degradation mechanisms of perovskite materials, it is crucial to observe their transitions on the atomic and sub-micrometer scales by EM. But as discussed above, it is challenging to observe the atomic structure of perovskite materials due to electron or ion beam damage. Comparison of standard TEM and cryo-EM with regard to beam induced damage in the perovskite materials is illustrated in Figure 6c.[104] In this research, $MAPbI_3$ nanowires (NWs) were used in order to maintain the sample thickness below 100 nm, required due to the absorbance of heavy atom Pb. In the standard TEM observation at room temperature, there were two problems for imaging perovskite NWs: beam damage and moisture exposure during sample transfer. Perovskite NWs quickly decompose into PbI_2 upon exposure to high electron dose (≈500 e^- $Å^{-2}$) due to the extreme electron beam sensitivity of the organic MA^+ cation (Figure 6c). During sample transfer to the TEM column, perovskite NWs were inevitably exposed to moist air even with minimized transfer time (<5 s). Even with the

© 2020 WILEY-VCH Verlag GmbH & Co. KGaA, Weinheim

low electron dose imaging (≈12 e^- $Å^{-2}$) to minimize the beam damage, surface roughening was observed, indicating surface degradation occurs during sample insertion displayed in Figure 6c. To overcome the electron beam and moisture sensitivity of perovskite materials, a plunge-freezing procedure was introduced, modified from cryo-EM methods used in biology research, to protect the perovskite materials in pristine or operation state for high-resolution imaging.[110] The plunge-freezing method first disperses perovskite NWs onto a TEM grid in an inert environment, where they are then plunge-frozen in liquid nitrogen. All the reactions between perovskite NWs and nitrogen or moisture were kinetically suppressed at the cryogenic temperature, therefore plunge-freezing process maintains the NWs' pristine state and structural information.

A typical cryohigh resolution TEM (HRTEM) image of $MAPbI_3$ NW exposed to an electron dose of ≈12 e^- $Å^{-2}$ is shown in Figure 6c. Noticeably, NWs imaged at cryogenic conditions have much smoother surfaces compared to those imaged under room temperature. In high resolution images of $MAPbI_3$ NWs, it was possible to classify individual $[PbI_6]^{4-}$ octahedral and MA^+ molecule columns. Contrary to previous observations of a phase transition from tetragonal to orthorhombic at ≈165 K,[111] HRTEM images of $MAPbI_3$ crystals showed no structural change. This may be due to the fast cooling of the plunge-freezing procedure which suggests that fast cooling can freeze the initial structural information and the state of tetragonal phase can be successfully preserved.

Cryogenic techniques have also been applied to SEM. Figure 6d shows SEM observations of an integrated photoabsorbing layer composed of $MAPbBr_3$ cubic perovskite crystals and PbS quantum dots (QDs). This configuration produces intermediate-band solar cells which have a band between the valence and conduction bands.[112] SEM images of this intermediate-band photoabsorbing layer indicate the presence of 100–200 nm perovskite cubic crystals (gray perovskite region) with the coexistence of PbS QDs (white regions) with the size of a few tens of nm. In this research, perovskite cubic crystals with a size from 100 to 200 nm and PbS QDs with a size of few tens of nm are both observed to be vulnerable to the electron beam damage. With aid of cryogenic temperatures (≈153 K) SEM images were achieved with less electron beam damage. Beyond the SEM observation for intermediate-band photoabsorbing layers, they also performed the TEM observation for the same composite. HRTEM observations show how spherical PbS QD particles (black regions) with the size from 3 to 15 nm were densely dispersed. At higher magnification, lattice fringes were resolved, matching the 0.34 nm of *d*-spacing with the (111) plane of PbS (black regions) cubic structure and 0.30 nm of *d*-spacing with (200) plane of $MAPbBr_3$ (gray region) tetragonal structure with less damage of electron beams. These results confirmed that the PbS QDs were well dispersed in the $MAPbBr_3$ perovskite matrix under the preserved conditions. Cryo-SEM is also recently applied to observe the wettability of perovskite precursor during the blade-coating process on top of the textured Si solar cells.[113] In this study, cryo-SEM reveals the important role of right amount of dimethyl sulfoxide in perovskite precursor to uniformly covering the textured Si top surface.

3.3. Application of Other Cryogenic Technique on Perovskite Materials

Some modified measurements or tools which can be performed inside or outside of EM have been applied with cryogenic configurations on perovskite materials. As depicted in **Figure 7**a, Hentz et al. reported the nanoscale observation for the local microstructure, composition, and optical properties in the $MAPbI_3$ perovskite film by using cryogenic low temperature cathodoluminescence in scanning TEM (CL-STEM), which collects optical excitations from energetic electrons interacting with a luminescent material.[115] However, the CL intensity at the room temperature was so low that the spectral response was not able to be distinguished enough to verify the ion segregation. That is because electron beam can induce destructive trap sites in perovskite materials driving nonradiative recombination. To maximize the CL yield, they performed low-temperature (93 K) panchromatic CL-STEM mapping by using a liquid nitrogen-filled cryoholder. Because the low temperature of cryoholder minimized the undesired nonradiative carrier recombination as generated from the electron beam radiation, the low temperature CL spectra were pronounced enough to resolve separated luminescence wavelengths. They revealed the local stoichiometric variation which implied that the inhomogeneous spatial distribution of luminescence intensity was a result of phase segregation in perovskite materials.

Beyond cryo-EM, the cryo-FIB has proven invaluable for characterizing degradation mechanisms or intrinsic properties of perovskite materials in atomistic scale. In the case of FIB-based sample preparation, conventional acceleration voltages (16–30 kV) and currents (>2.5 nA) that are used for materials can induce severe amorphization, chemical degradation, and structural changes to organic specimens such as perovskite materials.[116] Moreover, high energy Ga ions can become implanted, which may also adversely affect the surface chemistry of perovskite materials. Cryo-FIB is normally performed below 100 K, and considerably mitigates damage during FIB preparation. Rivas et al. demonstrated how cryo-FIB preparation can be used to diminish beam damage of halide perovskite material based solar cells for atom probe tomography (APT).[117] Here, a cryostage was used to decrease the temperature of the sample to 83 K and an in-house manufactured holder was designed for tilting the cryo-stage without damaging the SEM column pole piece as depicted in Figure 7b. Cryo-FIB milling was performed using 16 kV of accelerating voltage and variable currents from 0.13 nA to 45 pA, effectively minimizing Ga damage. The final milling step was performed with a reduced accelerating voltage of 5 kV to remove the severely damaged regions by Ga ions. As a result, it was found from mass spectra obtained by APT that halide ion loss, especially iodide ions, was mitigated by preventing the thermal and irradiation damage of the perovskite film from high energy Ga ions.

Cryogenic techniques have also been employed for non-EM-related characterization for perovskite materials for the purpose of suppressing the ion migration. For instance, an ionic transport triggered by light-illumination in perovskite materials is extremely difficult to be quantified because ionic

© 2020 WILEY-VCH Verlag GmbH & Co. KGaA, Weinheim

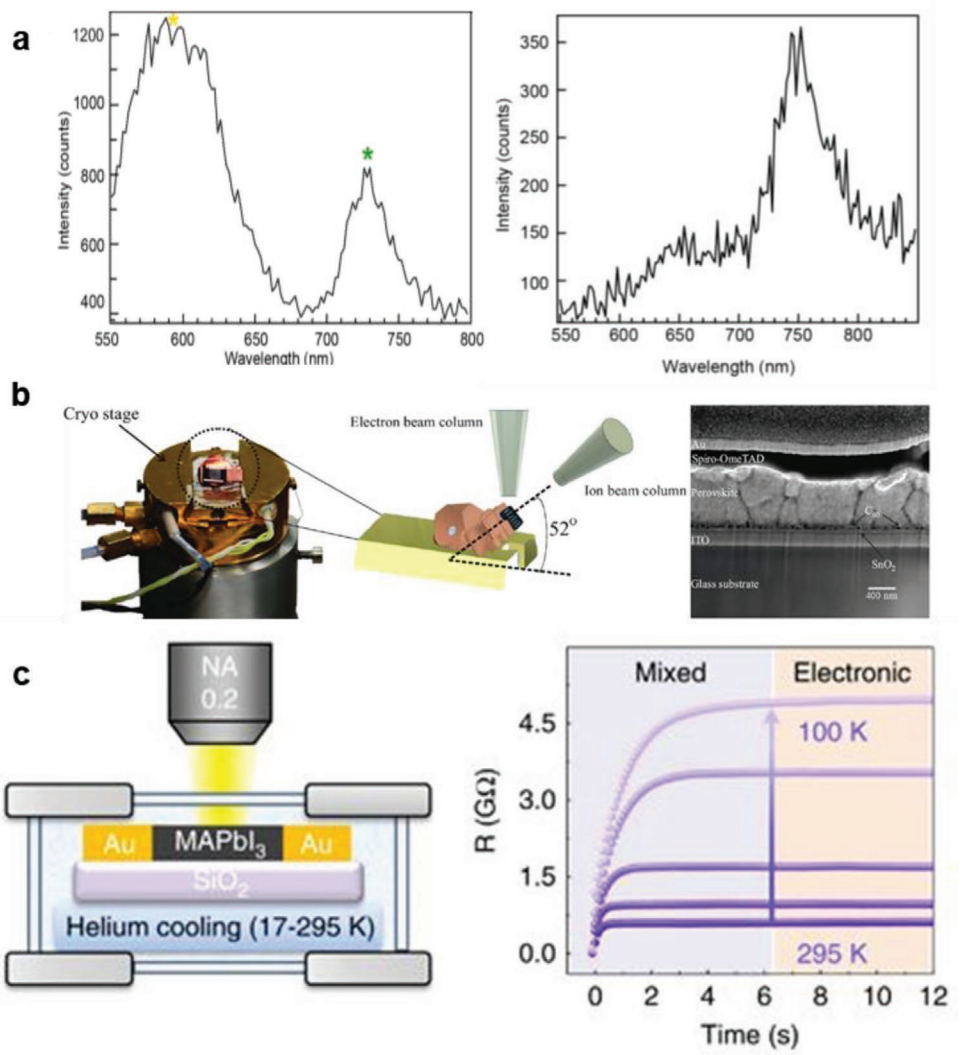

Figure 7. a) CL-STEM observation for phase separation in $MAPbI_3$ under cryotemperature (left) and room temperature (right). Reproduced with permission.[115] Copyright 2016, American Chemical Society. b) Lab-made cryo-FIB stage and schematics of usage (left). SEM image of PSC ($MAPbI_3$) prepared by cryo-FIB (right). Reproduced with permission.[117] Copyright 2020, PLoS. c) Schematic of cryogenic galvanostatic for perovskite lateral device ($MAPbI_3$) and five typical galvanostatic curves (resistance vs time) measured at different temperatures from 100 to 295 K. Reproduced with permission.[118] Copyright 2016, Springer Nature.

conductance is mixed with electronic contributions in photo-excited perovskite materials. By combining cryogenic galvanostatic and voltage–current measurements, Zhao et al. were able to demonstrate the quantification of light-enhanced ionic transport in $MAPbI_3$ film.[118] Because the ionic transport and electronic transport have different response to the low temperature, it was able to differentiate ionic relaxation and electronic resistance as depicted in Figure 7c. As a result, testing perovskite films over a wide range of temperatures (17–295 K) and light intensities (0–20 mW cm^{-2}) reveals a reduction in ionic transport activation energy by approximately a factor of five while under illumination. Likewise, application of cryogenic temperature assisted characterization has expanded a hidden range of comprehension for perovskite materials. Considering that cryogenic techniques are still developing, it is expected that further understanding of perovskite materials can be achieved with advancements in the near future.

4. In Situ Observations and Measurements

It is essential to obtain an in-depth understanding of the degradation mechanisms triggered by environmental exposure and thermal energies under realistic operating conditions to achieve the commercialization of PSCs. This requires an understanding of the relationship between the chemical and structural changes of the perovskite materials during photolysis, pyrolysis, or electrochemical processes in a working solar cell using various characterization techniques. Recently, remarkable progresses have been achieved in advanced characterization techniques for perovskite materials or solar cells under in situ conditions.[119–121] The term “in situ” means “in place” in Latin, and is used to describe a measurement emulating operating conditions. As such, in situ characterization can be used to more accurately describe mechanisms when compared to ex situ techniques. Although ex situ characterization techniques give

© 2020 WILEY-VCH Verlag GmbH & Co. KGaA, Weinheim

us enough valuable information about perovskite materials, characterizing the end product cannot provide the dynamic properties, such as the intermediate chemical and structural changes during operation under the light-illumination and heating. Moreover, due to their sensitivity to oxygen and moisture, perovskite materials can be continuously undergoing transitions which cannot be detected from ex situ characterization.

The performance of PSC is related to numerous features such as morphology, optoelectronic property (carrier generation and recombination), crystallinity.[122,123] First, the morphological changes are attributed to the chemical and structural changes of perovskite materials, and they can be studied by several in situ imaging techniques, which enables us to investigate microstructural transformations in high resolution.[124] In situ TEM and SEM measurements can reveal the morphological evolution of perovskite materials or carrier transporting materials with specific information of microstructural changes. Second, perovskite materials can be evaluated regarding photoabsorbing, carrier generation, and recombination capabilities.[125] In situ optoelectronic measurements can characterize the evolution of carrier dynamics inside of perovskite materials in accordance with electrochemical reactions while in operation. Last, ex situ X-ray assisted spectroscopies such as XRD, XPS, and XRF can characterize electronic and structural information of perovskite materials.[120] Though, the evolution of electronic and structural information can more accurately be measured by in situ X-ray assisted measurement tools, which are valuable characteristics to assess their performance and stability. In these regards, the development of the in situ characterization techniques applied into the perovskite materials will be introduced in the following sub-sections: in situ EM, in situ optoelectronic measurement, and in situ X-ray assisted measurement.

4.1. In Situ EM Characterization

Morphological and structural changes of perovskite materials can be analyzed by electron microscopy (SEM and TEM). SEM offers a better spatial resolution than optical microscope but not as good as TEM, therefore SEM is mostly used for tracking the morphological changes of perovskite thin film for optimizing the fabrication process.[126,127] Morphological variations can be easily tracked by dividing crystallization step via ex situ SEM techniques. An in situ EM observation for perovskite materials was first introduced in 2016 by Divitini et al. to study the impact of fabrication routes on thermal degradation of perovskite materials by using in situ TEM.[128] This was achieved with several advances in TEM technology at that time: the use of high brightness electron guns and detectors with large collection areas that allow the fast acquisition of EDS maps with low electron dose, and the development of novel in situ heating holders for TEM. The use of a low-dose electron beam is always suggested when characterizing beam-sensitive materials such as perovskite materials, and it was the key for developing in situ TEM characterization for perovskite materials. As a result of their efforts, the diffusion of heavy elements (lead and iodide) in perovskite materials into the Spiro-MeOTAD hole transporting materials could be seen in high-angle annular dark-field (HAADF) mode as the sample was heated (**Figure 8**a). By comparing quenching rates by in situ heating during HAADF measurements to control perovskite composition and morphology, they provided new insights of correlations between morphology (perovskite coverage and scaffold infiltration), chemical composition (Cl-containing or not), and thermal stability of perovskite materials. In the meantime, several different in situ TEM analyses for thermal degradation of perovskite materials were reported[129–131] as shown in Figure 8b,c, respectively. Such in situ TEM heating studies on perovskite materials demonstrated that in-depth understanding of thermal degradation routes and microstructural changes during the degradation can be achieved.

Another informative in situ observation which can be performed in TEMs involves applying electrical bias to the specimen. The pioneering work on in situ TEM analysis of perovskite materials under electrical bias was reported by Jeangros et al. in 2016 to study bias-induced nanoscale degradation mechanisms of $MAPbI_3$ perovskite materials.[132] As shown in **Figure 9**a, thin PSC lamella were prepared by FIB and cathode and anode components were attached to separated electrical contacts by Pt connections. The thin lamella was held under electrical biases of +6 and −6 V for 10 min, respectively, and the evolution of HAADF images with corresponding intensities were tracked as a function of time. As a result, there were bias-induced microstructural changes from the formation of PbI_2 nanoparticles and voids in perovskite thin lamella. Especially under the forward bias, the degradation of perovskite material occurred at the interface with the hole transport material, which suggested the need for analyzing the perovskite–hole transport material interactions during operation to improve the stability. Another application of in situ TEM, Jung et al. reported the observation of oxygen diffusion with biasing titanium oxide (TiO_2) based PSCs.[133] Previous work by Jeangros et al. required a large electrical bias (>6 V) to induce the current response through the TEM lamella due to the electrical connections through the highly resistive glass component (Figure 9b). However, for this work, Jung et al. required only 1 V to bias the sample by utilizing an in situ electrical biasing holder in TEM. After applying 1 V forward bias for an hour, the elemental distribution of the TEM sample measured by electron energy loss spectroscopy (EELS) showed the oxygen migration into the perovskite layer from the TiO_2 electron transport layer. These chemical and structural changes were proved to be partially reversible by applying a −1 V reverse bias (Figure 9c). This study revealed a new degradation mechanism of parasitic oxygen migration from the TiO_2 in the TiO_2 electron transport layer-based PSCs under electrical bias without any external sources such as moisture, oxygen, light, or thermal stress. Considering that the electron beam-induced damage may occur during in situ TEM observation, these studies discussed in this chapter provided either how they minimized the electron doses on their samples or reference in situ observation results without external stimuli that successfully exclude the beam-induced damage.

Although in situ TEM characterization tools provide important information on degradation mechanisms of perovskite materials as we have discussed in this section, external stimuli for in situ TEM experiments are currently limited to heating and electrical biasing due to the sensitivity of TEM systems

© 2020 WILEY-VCH Verlag GmbH & Co. KGaA, Weinheim

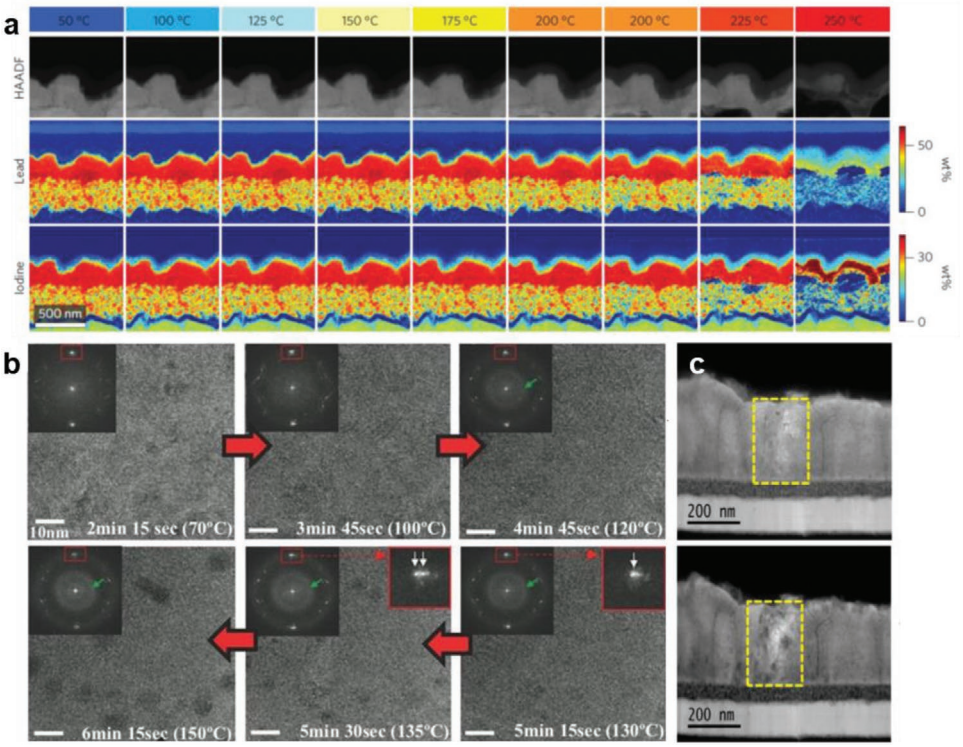

Figure 8. a) The evolution of HAADF image, lead and iodide composition of $MAPbI_3$ PSC depending on the temperature increase from 50 to 250 °C measured by in situ TEM observation for gradual thermal decomposition. Reproduced with permission.[128] Copyright 2016, Springer Nature. b) HRTEM images and corresponding FFTs for $MAPbI_3$ obtained from the in situ TEM under temperature increase from 70 to 150 °C. Reproduced with permission.[130] Copyright 2018, Wiley. c) HAADF images for $MAPbI_3$ obtained from the in situ TEM before heating (top) and after heating for 14 h (bottom). Reproduced with permission.[129] Copyright 2016, American Chemical Society.

which are easily effected by vacuum level, vibration, or contamination.[134] Looking toward the future, advanced in situ holders are needed which can produce controlled pressure with selected gases, or introduce the liquid into the TEM specimen in real time for the in-depth understanding on operational stability of PSCs.

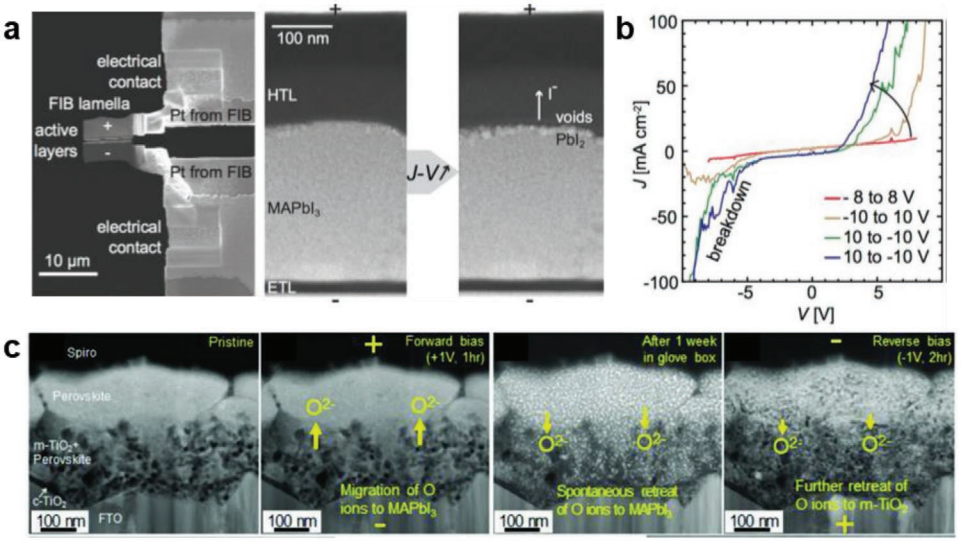

Figure 9. a) In situ TEM observation under electrical bias observing iodide anion migration and interfacial defect generation in $MAPbI_3$ PSC device and b) J–V measurements for the sample in (a) obtained in situ in the TEM. Reproduced with permission.[132] Copyright 2016, American Chemical Society. c) In situ TEM observation under 1 V of electrical forward bias for PSC device structure of FTO/TiO_2/$MAPbI_3$/Spiro-MeOTAD/Au observing oxygen anion migration into perovskite film. Reproduced with permission.[133] Copyright 2018, Wiley.

© 2020 WILEY-VCH Verlag GmbH & Co. KGaA, Weinheim

4.2. In Situ Optoelectronic Characterization

In situ characterization of optoelectronic properties in perovskite materials is as important as observing morphological/structural changes to elucidate the degradation mechanism and to improve the stability or performance of PSCs under real operation conditions. Carrier dynamics including the carrier generation from the photoincidence, carrier transport (extraction) to the electrode, and carrier recombination that can be evaluated by optoelectronic measurements such as photoluminescence (PL), electroluminescence (EL), current density–voltage (J–V) responses under various light source, Raman and UV–vis spectroscopy.[135–137] Beyond carrier dynamics, in situ optoelectronic measurements provide valuable information on the evolution of synthesis process, ion migration, or sample degradation.[119] Given the fact that most of perovskite thin film fabrication methods are based on spin-coating processes using chemical solution precursors, it is important to track the morphological/structural changes during the conversion process for optimizing film quality, and ultimately the performance of PSCs. Moreover, external stimuli (light, thermal stress, electrical bias) can provoke undesirable ion migration, phase transitions or decomposition. In situ optoelectronic studies, for that reasons, have been employed to investigate the evolution of carrier dynamics, formation, degradation, and ion movement within perovskite materials.

PL measurements are based on the observation of radiative recombination of carriers inside the materials which provides carrier dynamic information such as carrier generation, transportation and recombination. Bisquert et al. reported the electrical bias-induced state switching response of the PL in the $MAPbI_3$ perovskite layers with lateral symmetric electrodes measured by a wide-field PL imaging microscope as shown in **Figure 10**a.[138] Likewise, Deng et al. also reported the effects of light soaking on an operational PSC using in situ PL microscopy as depicted in Figure 10b.[139] Both works showed a decrease of PL intensity by external stimuli, but the former study observed that the electrical bias caused the decrease of PL intensity by a de-doping the migration of MA^+ and I^- ions and enhancing nonradiative recombination. On the other hand, the latter study used thermal stress as the external source and indicated the change of PL intensity is due to ion accumulation at the interfaces. Both studies provided crucial new insight into the correlation between the dynamics of charge carriers and mobile ions in operational PSCs.

KPFM has also recently been applied to perovskite materials to provide direct evidence correlating the morphology and electrical properties with the device performance. Ma et al. successfully adopted in situ KPFM for investigation on the local electrical properties of perovskite films with operating temperatures from 30 to 80 °C.[140] As shown in Figure 10c, the results indicate that the Fermi level of perovskite material continuously shifts down as the temperature rises, which implies the carriers within the film become slower with the higher temperature due to a decrease in the built-in electric field and enhancement of lattice vibration scattering. Because of findings on the evolution of carrier dynamics as thermal or light stimuli by in situ observation, better understanding of the operation of PSCs is reached.

In situ optoelectronic characterization tools can be also implemented to monitor and optimize the synthesis process for perovskite films fabricated from spin-coating or other solution process methods. Franeker et al. utilized in situ PL to monitor the thermal annealing process of perovskite films after spin-coating and found the best optimized performance of PSCs depending on annealing temperature and time.[141] Time-dependent PL intensities were monitored as a function of annealing temperature and quench rate (the higher annealing the temperature, the faster PL quench). An optimized annealing time occurred when the PL reached its baseline value as shown in **Figure 11**a. The authors suggested that changes in chemical composition and in crystallite habit and size accounted for these observations. As another example of using in situ optoelectronic characterization tools for monitoring the synthesis process, in situ UV–vis measurements were utilized to track time-resolved absorption spectra by Hu et al.[142] In this case, they investigated the drying kinetics of perovskite materials during the deposition with a blade-coater. Measuring the evolution of absorption spectra using in situ UV–vis, three distinguished stages were observed: no absorption, increased absorption, and stabilized absorption at a 500 nm wavelength. This indicated the process of nucleation and crystallization induced by the increasing concentration as a result from the solvent evaporation (Figure 11b). By comparing natural drying and air-knife-assisted drying processes, they found that the use of a nitrogen air-knife produces homogeneous, uniform films, leading to highly efficient, hysteresis-free PSCs with 20.26% of PCE by blade-coating. Last, application of in situ PL imaging was studied by Zhao et al., to investigate the perovskite crystallization process when the PbI_2 films were crystallized on perovskite seed crystals.[143] As can be seen in Figure 11c, two distinct types of crystal growth kinetics were captured in PL image: perovskite-seed-assisted growth (white circles) and the random nucleation (red dashed circles) without the seed layer. After only 13 s, the film was completely formed, shown in the last image of Figure 11c, indicating the fast growth of perovskite-seed-assisted fabrication method.

The use of in situ optoelectronic characterization tools are effective to study how the nucleation and the crystal growth occurred during the deposition and annealing processes of perovskite films and may guide the optimization of PSC device performance.

4.3. In Situ X-Ray Assisted Characterization

X-ray assisted characterization techniques have proven powerful tools for studying perovskite materials crystal structure, electronic structure, chemical composition, and morphology.[144] X-ray source can be easily adopted for in situ characterization techniques to monitor the evolution of materials under light illumination, thermal stress, or specific atmospheric conditions such as oxygen or moisture.[145–148] As with the aforementioned in situ characterization techniques for perovskite material studies, in situ X-ray assisted characterization tools can play complimentary roles to achieve better understanding and development of the material. Frequently utilized in situ X-ray techniques in perovskite research field are as follows: XRD,[149] XPS,[150] XRF,[151] and wide-angle X-ray scattering (WAXS).[15] As

© 2020 WILEY-VCH Verlag GmbH & Co. KGaA, Weinheim

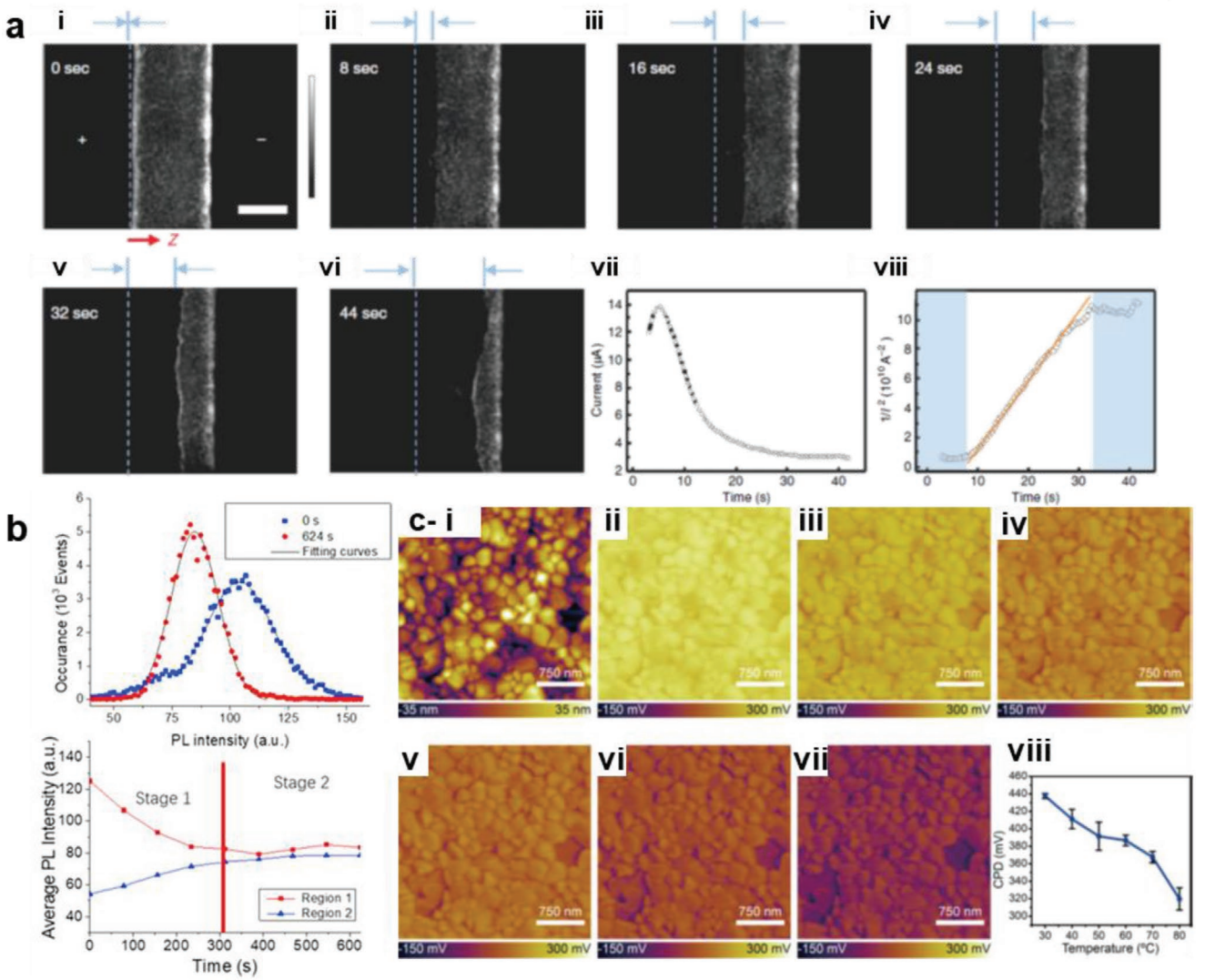

Figure 10. a-i–vi) In situ PL images of $MAPbI_{3-x}Cl_x$ perovskite film under electrical bias for 44 s. vii,viii) Electrical current (as a term of I and $1/I^2$) monitored as a function of time during the measurement. Reproduced with permission.[138] Copyright 2018, Springer Nature. b) (Top) Distribution of PL for $MAPbI_3$ perovskite film obtained from in situ PL measurement under continuous light illumination. Blue dots indicate PL before light illumination and red dots indicate PL after light illumination. (Bottom) Average PL intensity of different spot of the perovskite surface as a function of time. Reproduced with permission.[139] Copyright 2018, Elsevier. c-i) AFM topographic image of the $MAPbI_3$ perovskite films. CPD distributions of the $MAPbI_3$ perovskite films at ii) 30, iii) 40, iv) 50, v) 60, vi) 70, and vii) 80 °C obtained from in situ KPFM measurement. viii) Average CPD of the $MAPbI_3$ perovskite film as a function of temperature from 30 to 80 °C. Reproduced with permission.[140] Copyright 2019, American Chemical Society.

these techniques have the ability to evaluate chemical, structural, and morphological changes, they may be used to characterize states ranging from perovskite formation to degradation. Here in this chapter, actual application of these in situ X-ray assisted techniques will be discussed, especially for the evaluation of synthesis process and the mapping of structural and morphological changes of perovskite materials.

First, as X-ray assisted characterization tools may efficiently distinguish the stages of crystallization development during annealing steps in perovskite film fabrication, they were frequently employed to monitor the synthesis process.[5,152–155] For instance, Stone et al. used in situ XRD and XRF to reveal the perovskite formation mechanisms when using Cl-containing precursors by comparing the time dependence of chlorine intensity with the crystallinity of the perovskite at different annealing temperature.[156] **Figure 12**a shows the representative XRD reflections and a waterfall composite plot of in situ XRD which describes the evolution of perovskite films annealed at 100 °C measured by in situ XRD for 5, 30, and 70 min, respectively. As we can notice from the waterfall composite plot of in situ XRD in Figure 12b, the first step (up to 5 min) shows the crystallization of the precursor phase as the film dries, the second step (5–20 min) shows in latent stage the precursor scattering stayed constant without showing perovskite peak, and the last step (20–70 min) showed a continuous loss of precursor with the growth of the perovskite phase. By comparing in situ XRD and XRF, it was revealed that the onset of perovskite crystallization began when 50% of the Cl had evaporated from

© 2020 WILEY-VCH Verlag GmbH & Co. KGaA, Weinheim

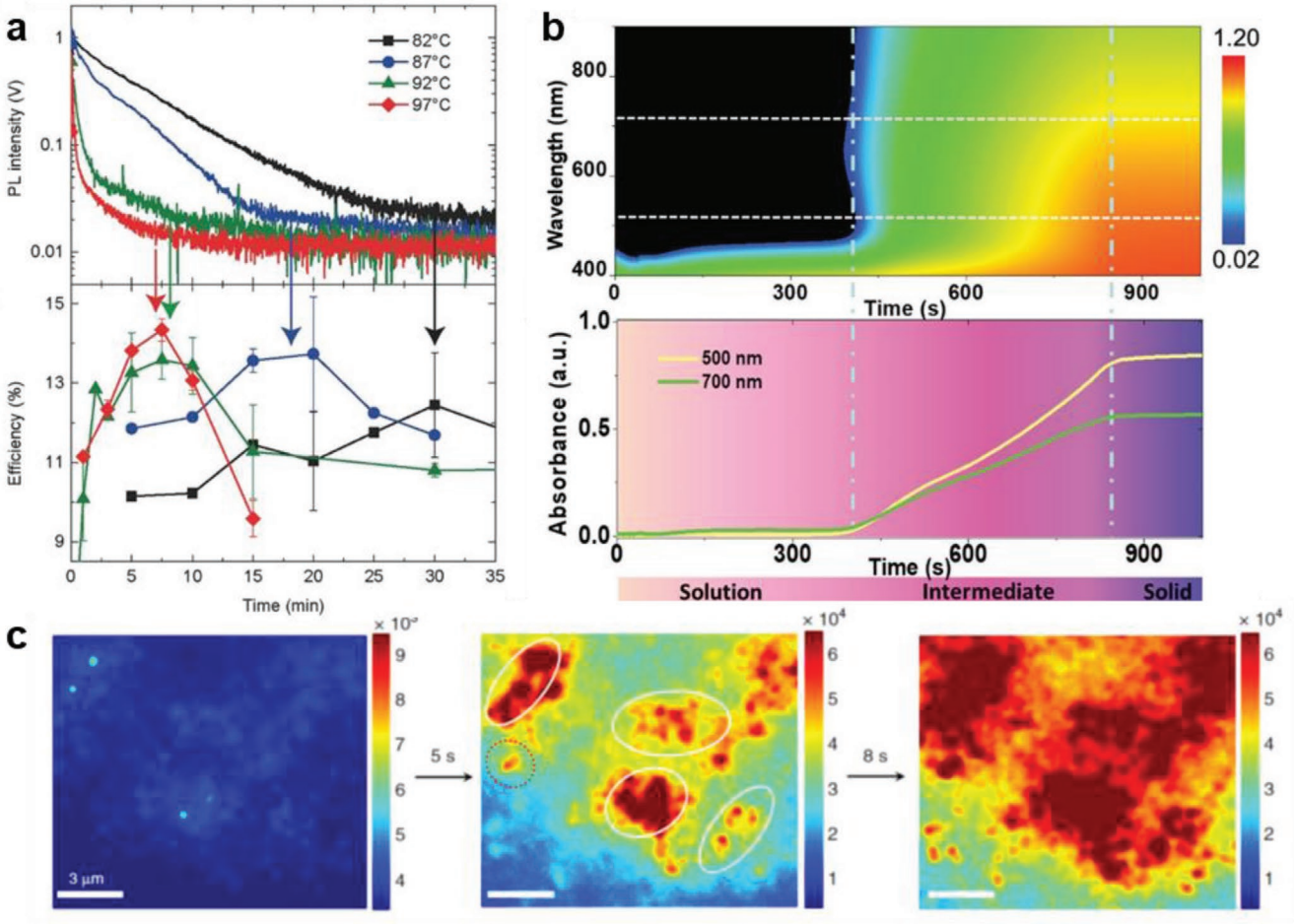

Figure 11. a) Evolution of the PL intensity and correlated power conversion efficiency of the $MAPbI_3$ perovskite devices depending on the annealing temperature and the time. Reproduced with permission.[141] Copyright 2016, Wiley. b) (Top) Time-resolved in situ UV–vis absorption spectra of natural drying $Cs_{0.05}FA_{0.81}MA_{0.14}PbI_{2.55}Br_{0.45}$ perovskite film by meniscus coating. (Bottom) Time-resolved absorbance at the wavelength of 500 and 700 nm, respectively. Reproduced with permission.[142] Copyright 2019, Wiley. c) Evolution of PL maps for $FAPbI_3$ based perovskite film taken from in situ PL imaging of the growth of perovskite seeded films. Reproduced with permission.[143] Copyright 2018, Springer Nature.

the film regardless of the annealing temperature from 95 to 105 °C (Figure 12b). As a result, they suggest a self-regulating model for transformation of Cl-containing perovskite film, suggesting that crystallization could begin after evaporation of MACl, depicted in Figure 12c. This transformative information of perovskite film could not have been realized with the ex situ XRD or XRF measurement for post-annealed sample. Using in situ X-ray assisted measurements to monitor the synthesis process of perovskite films, rapid development and optimization of device performances was achieved. At the same time, several studies using in situ grazing-incidence WAXS (GIWAXS) have also distinguished the stages of crystallization development during the perovskite film deposition (spin-coating or blade-coating) and annealing step.[157,158] For example, Zhong et al. reported the different solidification mechanisms of perovskite films deposited from spin-coating and blade-coating by tracking the crystallization process with in situ GIWAXS. They showed that film stabilization after the solvent drying occurred at 16.5 s for spin-coating and 250–300 s for blade-coating, which resulted in disordered precursor generating PbI_2-rich solvate and PbI_2 in the film from blade-coating. With the hot substrate (100–150 °C) for the rapid drying of the solvent, they were able to fabricate high-efficiency PSCs by blade-coating. Qin et al. studied mixed-perovskite ($FA_{0.83}MA_{0.17}Pb(I_{0.83}Br_{0.17})_3$) crystallization pathway during the spin-coating process with in situ GIWAXS by tracking the sample every 3 s. They revealed that mixed-perovskite spin-coating with antisolvent method has 3 different stages: 1) precursor, 2) δ-phase, 3) nonperovskite and intermediate phase. By adding Cs to the mixed-perovskite precursor, they were able to prevent the film from turning into stage 3 and achieve high efficiency mixed-PSC. In situ GIWAXS for perovskite materials normally requires synchrotron based X-ray sources as studies referred here because the scattering responses of the organic cations are weak.

Beyond characterization of the transformation of perovskite films, chemical/structural changes were pursued to observe ion migration under certain stimuli such as light, heat, electrical bias or introduction of gaseous molecules. Characterization of such stimuli can describe the enhancement[159,160] or degradation[161–163] in performance, and both can be efficiently measured with in situ X-ray assisted characterization tools. Enhancement in performance of perovskite film with continuous

© 2020 WILEY-VCH Verlag GmbH & Co. KGaA, Weinheim

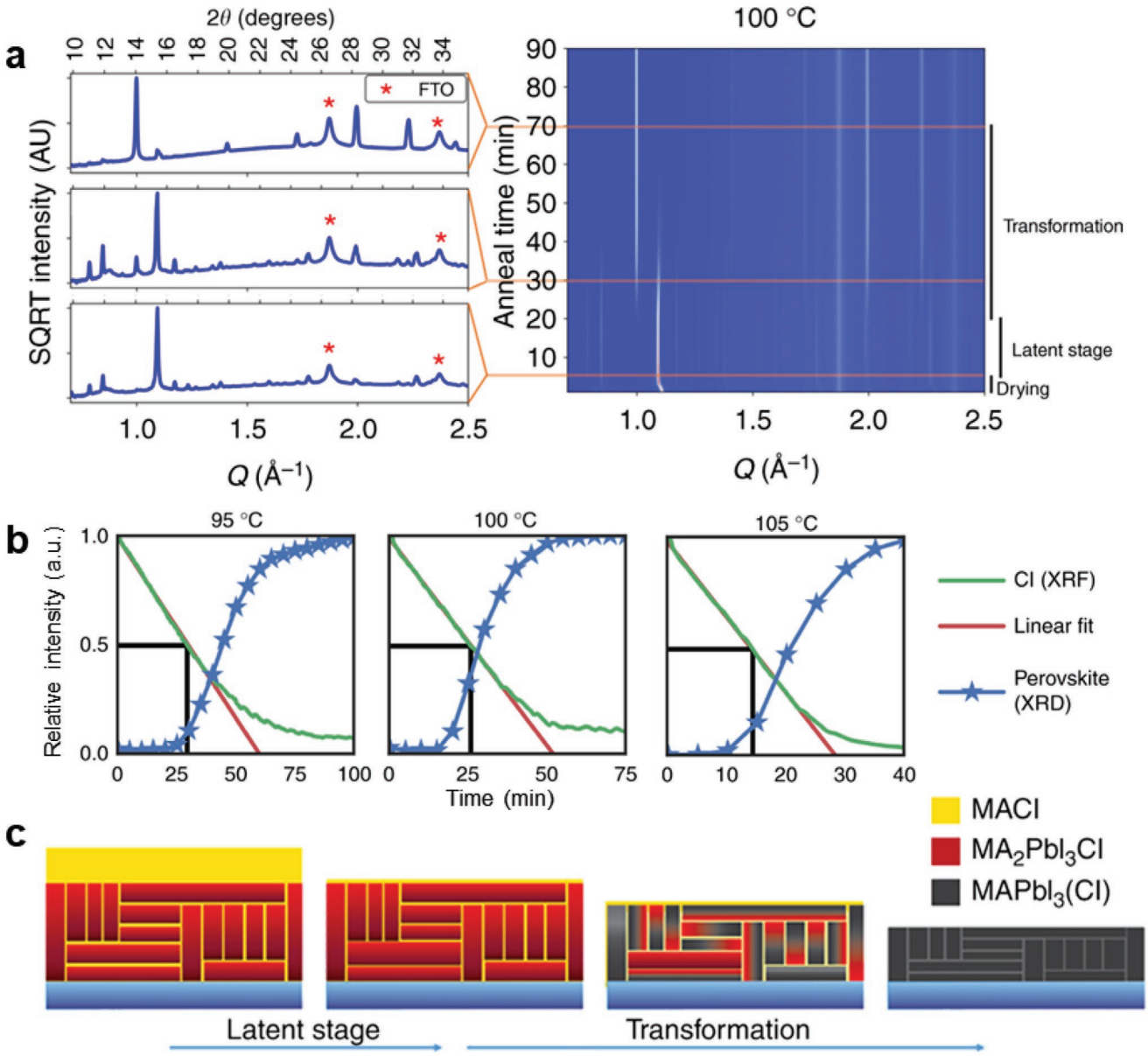

Figure 12. a) In situ XRD waterfall plots and representative XRD reflections (for 5, 30, and 70 min) of Cl-containing perovskite film annealed at 100 °C for 90 min. b) Change of Cl ratio inside of perovskite materials detected from in situ XRF. c) Suggested self-regulating model of the transformation from precursor to perovskite, indicating the loss of disordered MACl in the latent stage, followed by the crystallization with loss of MACl. Reproduced with permission.[156] Copyright 2018, Springer Nature.

light-illumination was reported by Tsai et al. which verified the beneficial effect of light-induced lattice expansion.[159] As can be seen in **Figure 13**a, grazing-incidence (GI) WAXS mapping was employed to measure the lattice parameter of perovskite crystals. With in situ GIWAXS, the time-dependent evolution of the lattice parameters was traced under continuous light-illumination which revealed continual lattice parameter expansion for 3 h (Figure 13b). This light-induced lattice expansion led to the relaxation of local lattice strain, which lowered the extraction barriers at interfaces, thereby showing a beneficial effect on the performance (especially V_{oc} and FF), as shown in Figure 13c. A representative study on degradation of perovskite materials using in situ X-ray tools is reported by Chen et al. to investigate photo- and moisture-dependent phase evolution.[163] Their lab-made in situ XRD equipment enclosed air with 65% relative humidity with an X-ray transparent window enabled the study of real-time photo- and moisture-triggered degradation of PSCs while operation, depicted in Figure 13d. By comparing the time-evolution of XRD reflection of the perovskite films with corresponding photovoltaic performance revealed the critical by-product that induced the performance degradation of PSCs (Figure 13e). At stage 1 (≈10 h), PCE dropped to around 73% of the initial PCE which corresponded to a decrease of XRD intensities of the $MAPbI_3$ peak which implies the formation of

© 2020 WILEY-VCH Verlag GmbH & Co. KGaA, Weinheim

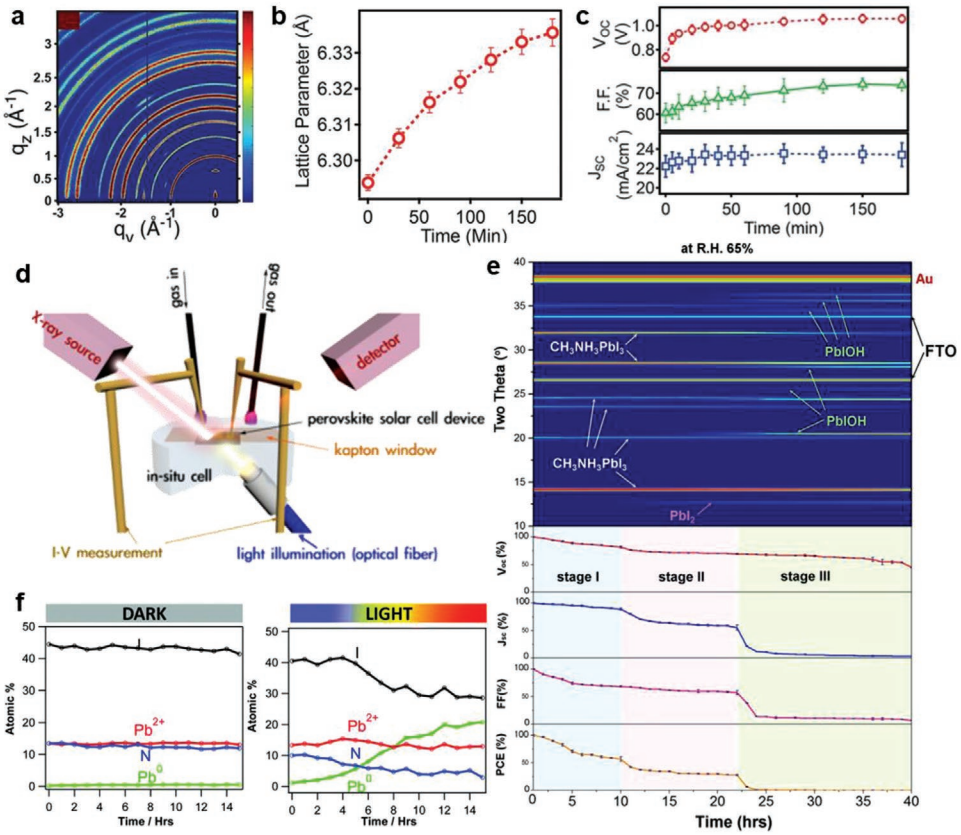

Figure 13. a) In situ GIWAXS plot of $FA_{0.7}MA_{0.25}Cs_{0.05}PbI_3$ perovskite materials with continuous light illumination b) Photoinduced lattice expansion as time and c) photovoltaic parameter enhancement. Reproduced with permission.[159] Copyright 2018, The American Association for the Advancement of Science. d,e) In situ XRD schematics and XRD reflections with corresponding performance variation to show 3 stage of degradation mechanism of $MAPbI_3$ PSCs. Reproduced with permission.[163] Copyright 2017, American Chemical Society. f) In situ XPS data for $MAPbI_3$ which shows the time-dependent variation of composition ions (I, Pb^{2+}, N, Pb^0) under light illumination. Reproduced with permission.[161] Copyright 2018, Royal Society of Chemistry.

$MAPbI_3 \cdot H_2O$ hydrate. PCE also significantly dropped at stage 2 (10–23 h) mainly with J_{sc} loss, where the in situ XRD experiment clearly indicated the formation of a PbI_2 phase. At stage 3 (≈23 h) a remarkable drop in J_{sc} and FF was observed, with a resulting PCE nearly 2% of initial performance. In situ XRD reflection illustrated that the PbIOH phase was produced at stage 3 which caused a severe degradation of perovskite materials. Similarly, Das et al. reported the time-evolution of the surface element ratio of $MAPbI_3$ perovskite layers under dark and light conditions in vacuum measured by in situ XPS to study the light-induced degradation mechanism (Figure 13f).[161] These unique findings on enhancement and degradation mechanisms of PSCs from in situ X-ray characterization provide profound understandings for changes of perovskite materials which cannot be taken from ex situ characterization tools.

5. Multidimensional Mapping Techniques

Multidimensional (2D or 3D) mapping techniques are important when characterizing perovskite film for a few reasons. First, perovskite exhibits a wide spatial variation both in vertical and lateral directions owing to several causes, including ion migration[42,164,165] and degradation.[166–168] It is widely accepted that perovskites are good ionic conductors since some anions (Br^-, I^-) and cations (MA^+, FA^+) can migrate within the film. As perovskite materials can be easily degraded from ambient atmosphere (oxygen and moisture)[169] and light,[170] the multidimensional analysis could provide direct insight into the nature of their ion migration and degradation propagation. Second, multidimensional mapping can probe subsurface properties which may not be fully understood with the investigation of surfaces only. Many characterization methods are utilized in a multidimensional approach to characterize the spatial variation of perovskite materials from micro- to nanometer scale.

2D mapping techniques are primarily applied to detect the areal distribution of chemical composition with optoelectronic, morphological, and carrier dynamic variations. 2D mapping of the film is achieved from characterization tools that provide spatial information from any type of source including light, X-ray, or e-beam with a combination of microscopic images.[171] EMs, including SEM and TEM, atomic force microscopy (AFM), or confocal laser microscopy (CLS) are the main tools for 2D mapping. EDS or EELS can be combined with EM to map the chemical evolution along the film. XRF also provides the chemical variation mapping with the area X-ray detector and fluorescence

© 2020 WILEY-VCH Verlag GmbH & Co. KGaA, Weinheim

detector. As perovskite materials are essentially utilized for solar applications, it is crucial to map the carrier dynamics and to correlate them with the spatial distribution of defect sites, morphologies, and chemical compositions. In that sense, mapping the PL of the perovskite provides carrier dynamics along the film.[172] Electron beam induced current (EBIC) or X-ray beam induced current (XBIC) measurements are also used to evaluate the spatial electrical properties of PSCs.

3D mapping can be achieved by reconstruction from multiple stacks of 2D images with the aid of proper ion-etching techniques.[173,174] This offers information in the *z*-direction while 2D mapping images only provide *x*–*y*-directional information, and is especially useful when it comes to studying the effect of degradation. Ion migration triggered degradation from the metal electrode or iodide can be assessed by depth profiling measurements with 3D mapping of ToF-SIMS or XPS. 3D reconstruction of morphological and compositional 2D information enables elucidation of degradation and defect behavior buried within perovskite films. Another possible way to obtain 3D spatial information is tomography, which has not been commonly used in PSC research field due to the limit of resolution. It is expected in the future that buried mechanism can be resolved with the aid of cryogenic tomography holders. In this section, we discuss some representative studies using 2D and 3D mapping techniques on perovskite materials.

5.1. 2D Mapping

2D mapping can detect and resolve spatial chemical, morphological, optoelectronic, electrical distribution of the perovskite film. PL is one of the most important 2D mapping characterization tools for investigating spatial optoelectronic properties of perovskite films. Since PL indicates where the radiative recombination occurs, it can be used to image the effects of spatial variation on carrier dynamics, including correlations of transport and recombination behavior in the presence grains or interfaces. Carrier dynamic investigations mainly rely on bulk PL response, because it is impossible to identify the local carrier dynamics before mapping the spatial PL distribution from the film. It was shown formerly by deQuilettes et al. that PL intensity and lifetime varied from grain to grain within the same perovskite film, while bulk films showed long carrier lifetime (**Figure 14**a).[175] They used confocal fluorescence microscopy with SEM to resolve the PL decay from perovskite films and revealed that higher concentration of chlorine made the PL brighter, and pyridine treatment could activate grains with dark PL response.

AFM and some of its extended techniques are commonly utilized for mapping the surface of the perovskite films. Standard AFM can map the morphological distribution of the film, while KPFM can map the work function or surface potential by measuring potential difference between the conductive AFM tip and the sample. In addition, conductive-AFM (c-AFM) enables collection of electrical data in nanoscale. Tennyson et al. used KPFM to investigate local potential variation in three samples with different compositions.[176] They designed the experiment to monitor V_{oc} under 1 sun illumination using a conductive Pt-coated Si probe as shown in Figure 14b. The result showed that Cs-incorporated perovskite had uniform spatial distribution of V_{oc} and reversible response to light exposures due to the suppression of ion motion resulting from crystal lattice shrinkage.

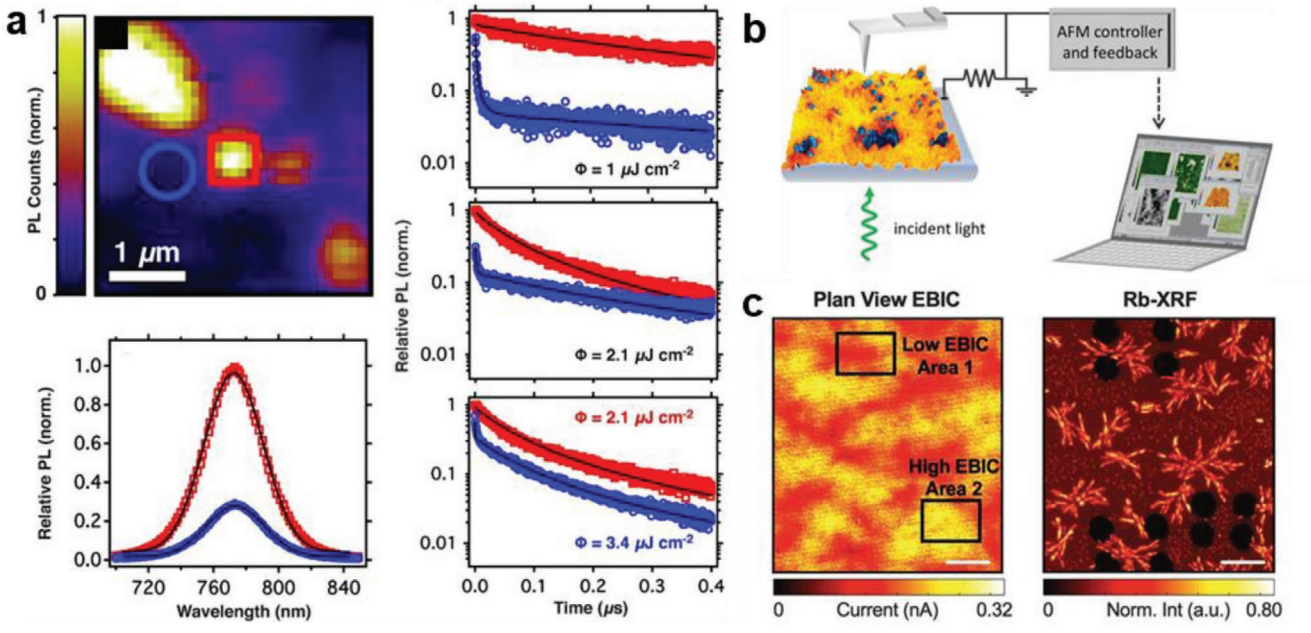

Figure 14. a) Plan view PL mapping of $MAPbI_3(Cl)$ perovskite and corresponding time-resolved PL spectra indicating inhomogeneity of perovskite film. Reproduced with permission.[175] Copyright 2015, The American Association for the Advancement of Science. b) Instrumental setup schematics for c-AFM 2D mapping for perovskite film. Reproduced with permission.[176] Copyright 2019, American Chemical Society. c) Plan view EBIC mapping and Rb-XRF mapping of Rb containing perovskite film. Reproduced with permission.[180] Copyright 2019, The American Association for the Advancement of Science.

© 2020 WILEY-VCH Verlag GmbH & Co. KGaA, Weinheim

On the other hand, $MAPbBr_3$ and $MAPbI_3$ demonstrated spatial inhomogeneity in V_{oc}, showing irreversible response upon multiple exposures to a light source. In 2014, Bergsmann et al. used KPFM to investigate the cross-sectional potential distribution in $MAPbI_3$ under illumination condition.[177] On illumination and short-circuit condition, charge carriers were generated in the absorber layer and holes were accumulated at the interfaces between the perovskite and HTL. These carrier dynamic changes induced the unbalanced charge distribution along the perovskite device, which was confirmed by KPFM in this study. The result revealed an electrical potential barrier was formed due to the accumulation of excessive holes and resulted in a reduced short-circuit current density. For the case of c-AFM, Kutes et al. used photoconductive AFM to map the spatial variation of $MAPbI_3$ solar cell performance.[178] They pointed out that PV performance varies significantly even in the same perovskite film by mapping the current of a HTL-free PSC (glass/FTO/TiO_2/$MAPbI_3$). The light was exposed through FTO/glass cathode and current was measured with a c-AFM probe at the anode simultaneously. The result revealed substantial current difference correlated with microstructural features.

One of the most successful attempts on interpreting 2D maps is to combine several techniques to confirm both chemical and optoelectronic properties at the same time, Luo et al., demonstrated that the region with higher bromide concentration showed better optoelectronic performance by combining XRF and PL mapping to detect chemical and optoelectronic distribution simultaneously.[179] They chose single crystal $MAPbBr_3$ as a sample to avoid the complication of considering grain boundaries and focused on direct correlation between Br concentration and PL intensity. While the sample was applied with lateral electrical bias of +2 V and −2 V, nanoprobe XRF (nano-XRF) was used to resolve the chemical composition and PL intensity was measured to compare optoelectronic enhancement. As a result, the region exposed to higher potential showed an increase in PL intensity and Br concentration which suggested that Br ion can easily migrate inside the film and can be correlated with optoelectronic performance enhancement. Likewise, another work combined nano-XRF and EBIC to illustrate the negative correlation between charge collection and Rb concentration by showing that regions of lower EBIC corresponded to higher Rb concentrations as depicted in Figure 14c.[180] However, low EBIC region were broader than the high Rb region in XRF. They attributed this mismatch to larger carrier generation volume from electron beam compared to nano-XRF probe. Another possible explanation was carrier diffusion and successive recombination near Rb aggregates. Recently, AFM and nano-FTIR were conducted to correlate chemical phases in individual grains in CsFAMA perovskite films.[181] The regions showing strong IR activity were depleted with FA vibrational modes, which indicated grains with FA deficient compositions show stronger vibrational response.

5.2. 3D Mapping

Mapping techniques play a crucial role in studying degradation mechanisms. Since PSCs consist of several different layers, it is important to measure the composition or charge distribution along the z direction. Domanski et al. reported on how the gold contact material diffuses into the perovskite layer using ToF-SIMS.[182] They used elemental depth-profiling techniques to measure the concentration of Au across the device and reconstructed elemental 3D maps. It was clear that Au atoms migrated from the back-contact layer to perovskite layer as shown in **Figure 15**a. They suggested that the Au migration into

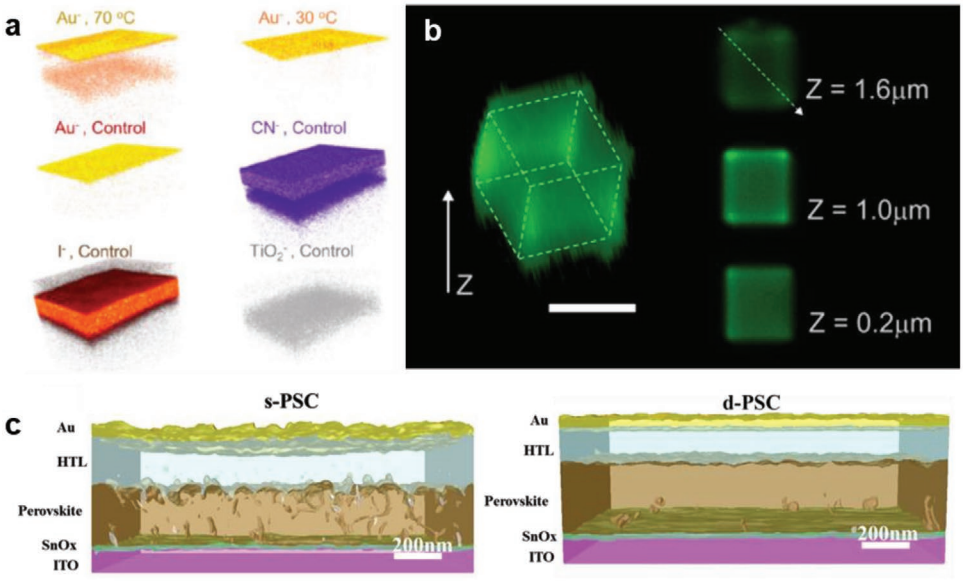

Figure 15. a) 3D mapping of ToF-SIMS showing metal electrode (Au) migration into perovskite internal layer (I^-) penetrating the hole transport materials (CN^-) depending on the temperature. Reproduced with permission.[182] Copyright 2016, American Chemical Society. b) 3D PL reconstruction of $MAPbBr_3$ perovskite cube with PL images taken at several vertical positions of the microstructure. Scale bar is 2 μm. Reproduced with permission.[185] Copyright 2016, American Chemical Society. c) 3D reconstruction images from the assist of FIB/SEM for the $MAPbI_3$ PSCs with static-spin-coated HTL (s-PSC), and dynamic-spin-coated HTL (d-PSC). Reproduced with permission. Copyright 2020, Elsevier.

© 2020 WILEY-VCH Verlag GmbH & Co. KGaA, Weinheim

the perovskite layer led to severe degradation in V_{oc} and J_{sc} at the high temperature which could be successfully mitigated by insertion of a thin Cr layer deposited between HTL and Au contact layer.

Another study regarding humidity-driven perovskite degradation using 3D mapping by ToF-SIMS was conducted in 2017 by Lin et al.[183] The researchers monitored water penetration into perovskite films, using an isotope of H_2O, deuterium oxide (D_2O). They made an 84% relative humidity environment with D_2O and exposed the sample to the environment for 1–30 days. After 1–3 days, aggregation of deuterium was observed at the perovskite surface and byproducts (CH_3NH_2D, CH_3NHD_2, and CH_3ND_3) were formed from proton exchange reactions between MAI and deuterium. Eventually, these molecules were transformed to CH_3NH_2(or CH_3ND_2) and were eliminated by evaporation. This detachment of organic compounds induced perovskite crystal structure distortion. They confirmed their hypothesis via monitoring CH_3NH_3 molecules for 30 days. On the first day, the majority of CH_3NH_3 molecules were present at the surface. After five days, CH_3NH_3 decreased drastically and was nearly completely depleted at the surface and only small amount were detected at the bottom. After 12–30 days CH_3NH_3 was almost under the detection limit. The result provided a direct observation of perovskite decomposition from humidity exposure. Meanwhile, another study reported the 3D mapping of adsorbed water in perovskite solar cells which indicated that the HTL prefers to adsorb water due to the hygroscopicity of additive in the HTL.[184] This study provided that the correlation of humidity-driven degradation of perovskite materials and the HTL.

Also, 2D PL maps can be reconstructed into 3D maps to investigate the optoelectronic spatial distribution as can be seen in Figure 15b.[185] Photoinduced degradation was studied by Galisteo-Lopez et al. using 3D PL mapping technique. They selectively exposed intense light (14.2 W cm^{-2}) to $MAPbBr_3$ and measured 2D PL intensity along the *xy* plane. Afterward, they stacked the PL images to make a 3D structure to investigate the effect of photodegradation along *x*, *y*, and *z* directions. The result showed that the illuminated region with very low PL intensity and the unexposed region remain bright in PL images. Moreover, it was not just remaining bright but the intensity of PL in unexposed area increased whereas exposed area decreased. The PL peak position of illuminated region blue-shifted compared to the unexposed region which indicated that the bandgap increased with bromide concentration. They also conducted SEM and EDS to investigate the structural and compositional changes in the illuminated sample. The photo-exposed region showed lower halide concentration with respect to unexposed portion. Combining these results, this work suggested that halide migration induces defects lattice distortion.

Morphological 3D reconstruction mapping also provides the valuable information during the fabrication or degradation of PSCs. Shen et al. studied chemical and morphological variations for PSCs with static spin-coated HTLs (s-PSC) and with dynamic spin-coated HTLs (d-PSC) by 3D reconstruction with FIB/SEM.[186] The spin-coating process for s-PSC contains the wetting process of HTL solution on the top of the perovskite film, while d-PSC can be performed without chlorobenzene wetting on the perovskite film. As displayed in Figure 15c, morphological differences of using static and dynamic HTL spin-coating onto the perovskite film can be distinguished by 3D mapping reconstructed from FIB/SEM. It was discovered that the s-PSC device showed critical void generation along the perovskite layers due to the reaction between perovskite materials and detrimental additives in Spiro-MeOTAD.

6. Conclusions and Outlook

In this article, we have reviewed the present challenges that perovskite materials exhibit intrinsically and extrinsically, and advanced characterization methods such as cryotechniques, in situ measurements, and multidimensional imaging and mapping tools, which contribute the proper characterization of perovskite materials. Fast ionic movement and vulnerability to degradation and phase transition were main factors to impede accurate characterization of perovskite materials. Perovskite materials can be detrimentally affected by the high energy probes including lasers, e-beams, and X-rays, required by the majority of characterization tools. Considering that perovskite materials are also vulnerable to the thermal stress, moisture, and pressure, driving degradation or phase transition, we emphasize the significance of controlled measurement conditions. Rapid ion mobility and their accumulations are also a critical hinderance to accurate characterization due to continuous variation of the result with the time and the space.

Employing advanced characterization tools can surmount such challenges for perovskite materials. Degradation due to measurement source radiation and accompanied heat generation can be mitigated with cryotemperature techniques, and cryo-FIB and -EM have been successfully adopted to investigate the micro-/nanostructure of perovskite materials. Cryo-techniques can even freeze the phase of perovskite materials with the instantaneous cooling process, thereby the preventing phase transitions during the measurements. Time-dependent variation with the temperature, light exposure, or other stimuli that may influence the perovskite materials can be tracked by in situ measurement techniques. In situ EM, optoelectronic measurements, and X-ray assisted tools effectively track the time-dependent microstructural, carrier dynamical, chemical variations of perovskite materials. Lastly, spatial distribution of intrinsic properties due to ion migration or phase separation can be resolved with 2D mapping, and the 3D reconstruction of the 2D map stacks provide the valuable information of buried internal distributions, effectively correlating electronic effects with structural features.

Pioneering studies for overcoming the challenges of perovskite materials have achieved developments on appropriate characterizations and have corrected decisive misinterpretations of the materials as well. However, current advanced characterization tools still have remaining unsolved problems. For cryotemperature methods, possible undesirable phase transitions during long-term measurements may occur at low temperature which are not yet fully understood due to a lack of exploration of low temperature phase transitions. Disparity between actual operational mechanisms of PSCs and the implementation of in situ measurements may limit the understanding on the stability issue under actual operation, emphasizing the importance of

© 2020 WILEY-VCH Verlag GmbH & Co. KGaA, Weinheim

experimental design. These differences should be minimized to appropriately explain the degradation mechanism during the operation from in situ observation. For multidimensional mapping characterization, resolution can be problematic for interpretation of spatial variations. These problems arise because the current perovskite characterization tools are mostly adopted from parent photovoltaics or traditional inorganic perovskite research. There are efforts to develop new emerging characterization techniques for PSC materials such as photoemission electron microscopy (PEEM)[187] or drive-level capacitance profiling (DLCP)[188], which broaden the comprehension on PSC materials. PEEM can image the nanoclustered trap sites in perovskite films which is formerly predicted from PL mapping. PEEM provides far more accurate location of trap sites than PL because photoexcited carriers in the bulk can diffuse along with the perovskite film and detected at the surface. DLCP can directly resolve the free carrier density and trap density and its spatial distribution. It was discovered that trap states mostly exist at the interface from the measured spatial distribution of trap states at bulk and interface of single- or polycrystalline perovskite film. In this regard, proper optimization of characterization tools for the perovskite research is required to understand perovskite materials further.

Acknowledgements

This work was supported by California Energy Commission EPIC Advance Breakthrough Award (EPC-16-050). This work was also supported by the Basic Science Research Program through the National Research Foundation of Korea (NRF) funded by the Ministry of Education (2019R1A6A3A12031412). The authors would like to acknowledge financial support received for this study from the U.S. Department of Energy, Office of Basic Energy Sciences, under Award Number DE-SC0002357 (program manager Dr. Jane Zhu).

Conflict of Interest

The authors declare no conflict of interest.

Keywords

characterization, cryogenic electron microscopy, in situ measurements, multidimensional mapping, perovskite solar cells

Received: May 26, 2020
Revised: June 29, 2020
Published online:

[1] O. Ellabban, H. Abu-Rub, F. Blaabjerg, *Renewable Sustainable Energy Rev.* **2014**, *39*, 748.
[2] N. S. Lewis, *Science* **2007**, *315*, 798.
[3] J. Burschka, N. Pellet, S. J. Moon, R. Humphry-Baker, P. Gao, M. K. Nazeeruddin, M. Gratzel, *Nature* **2013**, *499*, 316.
[4] J. H. Im, C. R. Lee, J. W. Lee, S. W. Park, N. G. Park, *Nanoscale* **2011**, *3*, 4088.
[5] N. J. Jeon, J. H. Noh, Y. C. Kim, W. S. Yang, S. Ryu, S. I. Seok, *Nat. Mater.* **2014**, *13*, 897.
[6] A. Kojima, K. Teshima, Y. Shirai, T. Miyasaka, *J. Am. Chem. Soc.* **2009**, *131*, 6050.
[7] M. M. Lee, J. Teuscher, T. Miyasaka, T. N. Murakami, H. J. Snaith, *Science* **2012**, *338*, 643.
[8] W. S. Yang, J. H. Noh, N. J. Jeon, Y. C. Kim, S. Ryu, J. Seo, S. I. Seok, *Science* **2015**, *348*, 1234.
[9] H. S. Kim, C. R. Lee, J. H. Im, K. B. Lee, T. Moehl, A. Marchioro, S. J. Moon, R. Humphry-Baker, J. H. Yum, J. E. Moser, M. Gratzel, N. G. Park, *Sci. Rep.* **2012**, *2*, 591.
[10] National Renewable Energy Laboratory (NREL), Best Research-Cell Efficiency Chart, https://www.nrel.gov/pv/cell-efficiency.html (accessed: April 2020).
[11] M.-c. Kim, N. Ahn, E. Lim, Y. U. Jin, P. V. Pikhitsa, J. Heo, S. K. Kim, H. S. Jung, M. Choi, *J. Mater. Chem. A* **2019**, *7*, 12075.
[12] M. Park, W. Cho, G. Lee, S. C. Hong, M. c. Kim, J. Yoon, N. Ahn, M. Choi, *Small* **2019**, *15*, 1804005.
[13] G. Grancini, C. Roldan-Carmona, I. Zimmermann, E. Mosconi, X. Lee, D. Martineau, S. Narbey, F. Oswald, F. De Angelis, M. Graetzel, M. K. Nazeeruddin, *Nat. Commun.* **2017**, *8*, 15684.
[14] Z. Li, T. R. Klein, D. H. Kim, M. Yang, J. J. Berry, M. F. A. M. van Hest, K. Zhu, *Nat. Rev. Mater.* **2018**, *3*, 1.
[15] H. Tsai, W. Nie, J. C. Blancon, C. C. Stoumpos, R. Asadpour, B. Harutyunyan, A. J. Neukirch, R. Verduzco, J. J. Crochet, S. Tretiak, L. Pedesseau, J. Even, M. A. Alam, G. Gupta, J. Lou, P. M. Ajayan, M. J. Bedzyk, M. G. Kanatzidis, *Nature* **2016**, *536*, 312.
[16] K. A. Bush, A. F. Palmstrom, Z. J. Yu, M. Boccard, R. Cheacharoen, J. P. Mailoa, D. P. McMeekin, R. L. Z. Hoye, C. D. Bailie, T. Leijtens, I. M. Peters, M. C. Minichetti, N. Rolston, R. Prasanna, S. Sofia, D. Harwood, W. Ma, F. Moghadam, H. J. Snaith, T. Buonassisi, Z. C. Holman, S. F. Bent, M. D. McGehee, *Nat. Energy* **2017**, *2*, 1.
[17] J. A. Christians, P. Schulz, J. S. Tinkham, T. H. Schloemer, S. P. Harvey, B. J. T. de Villers, A. Sellinger, J. J. Berry, J. M. Luther, *Nat. Energy* **2018**, *3*, 68.
[18] National Renewable Energy Laboratory (NREL), Champion Photovoltaic Module Efficiency Chart, https://www.nrel.gov/pv/module-efficiency.html (accessed: April 2020).
[19] J. H. Noh, S. H. Im, J. H. Heo, T. N. Mandal, S. I. Seok, *Nano Lett.* **2013**, *13*, 1764.
[20] M. C. Kim, B. J. Kim, D. Y. Son, N. G. Park, H. S. Jung, M. Choi, *Nano Lett.* **2016**, *16*, 5756.
[21] S. D. Stranks, G. E. Eperon, G. Grancini, C. Menelaou, M. J. Alcocer, T. Leijtens, L. M. Herz, A. Petrozza, H. J. Snaith, *Science* **2013**, *342*, 341.
[22] J. De Roo, M. Ibanez, P. Geiregat, G. Nedelcu, W. Walravens, J. Maes, J. C. Martins, I. Van Driessche, M. V. Kovalenko, Z. Hens, *ACS Nano* **2016**, *10*, 2071.
[23] J. You, L. Meng, T. B. Song, T. F. Guo, Y. M. Yang, W. H. Chang, Z. Hong, H. Chen, H. Zhou, Q. Chen, Y. Liu, N. De Marco, Y. Yang, *Nat. Nanotechnol.* **2016**, *11*, 75.
[24] Z. Xiao, Y. Yuan, Y. Shao, Q. Wang, Q. Dong, C. Bi, P. Sharma, A. Gruverman, J. Huang, *Nat. Mater.* **2015**, *14*, 193.
[25] E. L. Unger, A. R. Bowring, C. J. Tassone, V. L. Pool, A. Gold-Parker, R. Cheacharoen, K. H. Stone, E. T. Hoke, M. F. Toney, M. D. McGehee, *Chem. Mater.* **2014**, *26*, 7158.
[26] X. Li, M. I. Dar, C. Yi, J. Luo, M. Tschumi, S. M. Zakeeruddin, M. K. Nazeeruddin, H. Han, M. Grätzel, *Nat. Chem.* **2015**, *7*, 703.
[27] J. H. Kim, C. C. Chueh, S. T. Williams, A. K. Jen, *Nanoscale* **2015**, *7*, 17343.
[28] D. G. Lee, M.-c. Kim, B. J. Kim, D. H. Kim, S. M. Lee, M. Choi, S. Lee, H. S. Jung, *Appl. Surf. Sci.* **2019**, *477*, 131.
[29] Y. Zhou, H. Sternlicht, N. P. Padture, *Joule* **2019**, *3*, 641.
[30] L.-L. Gao, L.-S. Liang, X.-X. Song, B. Ding, G.-J. Yang, B. Fan, C.-X. Li, C.-J. Li, *J. Mater. Chem. A* **2016**, *4*, 3704.

 © 2020 WILEY-VCH Verlag GmbH & Co. KGaA, Weinheim

[31] A. Sharenko, C. Mackeen, L. Jewell, F. Bridges, M. F. Toney, *Chem. Mater.* **2017**, *29*, 1315.
[32] B. Yang, W. Ming, M. H. Du, J. K. Keum, A. A. Puretzky, C. M. Rouleau, J. Huang, D. B. Geohegan, X. Wang, K. Xiao, *Adv. Mater.* **2018**, *30*, e1705801.
[33] J. S. Manser, J. A. Christians, P. V. Kamat, *Chem. Rev.* **2016**, *116*, 12956.
[34] Y. Zhao, K. Zhu, *Chem. Soc. Rev.* **2016**, *45*, 655.
[35] N. Klein-Kedem, D. Cahen, G. Hodes, *Acc. Chem. Res.* **2016**, *49*, 347.
[36] C. Xiao, Z. Li, H. Guthrey, J. Moseley, Y. Yang, S. Wozny, H. Moutinho, B. To, J. J. Berry, B. Gorman, Y. Yan, K. Zhu, M. Al-Jassim, *J. Phys. Chem. C* **2015**, *119*, 26904.
[37] J. D. McGettrick, K. Hooper, A. Pockett, J. Baker, J. Troughton, M. Carnie, T. Watson, *Mater. Lett.* **2019**, *251*, 98.
[38] D. Bryant, N. Aristidou, S. Pont, I. Sanchez-Molina, T. Chotchuna ngatchaval, S. Wheeler, J. R. Durrant, S. A. Haque, *Energy Environ. Sci.* **2016**, *9*, 1655.
[39] H. S. Kim, I. H. Jang, N. Ahn, M. Choi, A. Guerrero, J. Bisquert, N. G. Park, *J. Phys. Chem. Lett.* **2015**, *6*, 4633.
[40] H. J. Snaith, A. Abate, J. M. Ball, G. E. Eperon, T. Leijtens, N. K. Noel, S. D. Stranks, J. T. Wang, K. Wojciechowski, W. Zhang, *J. Phys. Chem. Lett.* **2014**, *5*, 1511.
[41] H. S. Kim, I. Mora-Sero, V. Gonzalez-Pedro, F. Fabregat-Santiago, E. J. Juarez-Perez, N. G. Park, J. Bisquert, *Nat. Commun.* **2013**, *4*, 2242.
[42] P. Calado, A. M. Telford, D. Bryant, X. Li, J. Nelson, B. C. O'Regan, P. R. Barnes, *Nat. Commun.* **2016**, *7*, 13831.
[43] N. Aristidou, C. Eames, I. Sanchez-Molina, X. Bu, J. Kosco, M. S. Islam, S. A. Haque, *Nat. Commun.* **2017**, *8*, 15218.
[44] E. J. Juarez-Perez, R. S. Sanchez, L. Badia, G. Garcia-Belmonte, Y. S. Kang, I. Mora-Sero, J. Bisquert, *J. Phys. Chem. Lett.* **2014**, *5*, 2390.
[45] C. Quarti, E. Mosconi, J. M. Ball, V. D'Innocenzo, C. Tao, S. Pathak, H. J. Snaith, A. Petrozza, F. De Angelis, *Energy Environ. Sci.* **2016**, *9*, 155.
[46] M. De Bastiani, G. Dell'Erba, M. Gandini, V. D'Innocenzo, S. Neutzner, A. R. S. Kandada, G. Grancini, M. Binda, M. Prato, J. M. Ball, M. Caironi, A. Petrozza, *Adv. Energy Mater.* **2016**, *6*, 1501453.
[47] C. Eames, J. M. Frost, P. R. Barnes, B. C. O'Regan, A. Walsh, M. S. Islam, *Nat. Commun.* **2015**, *6*, 7497.
[48] A. M. A. Leguy, Y. Hu, M. Campoy-Quiles, M. I. Alonso, O. J. Weber, P. Azarhoosh, M. Van Schilfgaarde, M. T. Weller, T. Bein, J. Nelson, P. Docampo, P. R. F. Barnes, *Chem. Mater.* **2015**, *27*, 3397.
[49] G. Y. Kim, A. Senocrate, T. Y. Yang, G. Gregori, M. Gratzel, J. Maier, *Nat. Mater.* **2018**, *17*, 445.
[50] N. Ahn, K. Kwak, M. S. Jang, H. Yoon, B. Y. Lee, J. K. Lee, P. V. Pikhitsa, J. Byun, M. Choi, *Nat. Commun.* **2016**, *7*, 13422.
[51] N. Aristidou, I. Sanchez-Molina, T. Chotchuangchutchaval, M. Brown, L. Martinez, T. Rath, S. A. Haque, *Angew. Chem., Int. Ed. Engl.* **2015**, *54*, 8208.
[52] G. Niu, X. Guo, L. Wang, *J. Mater. Chem. A* **2015**, *3*, 8970.
[53] E. J. Juarez-Perez, Z. Hawash, S. R. Raga, L. K. Ono, Y. Qi, *Energy Environ. Sci.* **2016**, *9*, 3406.
[54] L. Ma, D. Guo, M. Li, C. Wang, Z. Zhou, X. Zhao, F. Zhang, Z. Ao, Z. Nie, *Chem. Mater.* **2019**, *31*, 8515.
[55] H. P. Klug, L. E. Alexander, *X-Ray Diffraction Procedures: For Polycrystalline and Amorphous Materials*, 2nd ed. (Eds: H. P. Klug, L. E. Alexander), Wiley-VCH, Weinheim **1974**, p. 992.
[56] N. S. McIntyre, D. G. Zetaruk, *Anal. Chem.* **1977**, *49*, 1521.
[57] O. Cheshnovsky, S. H. Yang, C. L. Pettiette, M. J. Craycraft, Y. Liu, R. E. Smalley, *Chem. Phys. Lett.* **1987**, *138*, 119.
[58] S.-T. Ha, C. Shen, J. Zhang, Q. Xiong, *Nat. Photonics* **2016**, *10*, 115.
[59] T. Leijtens, E. T. Hoke, G. Grancini, D. J. Slotcavage, G. E. Eperon, J. M. Ball, M. De Bastiani, A. R. Bowring, N. Martino, K. Wojciechowski, M. D. McGehee, H. J. Snaith, A. Petrozza, *Adv. Energy Mater.* **2015**, *5*, 1500962.
[60] R. L. Z. Hoye, P. Schulz, L. T. Schelhas, A. M. Holder, K. H. Stone, J. D. Perkins, D. Vigil-Fowler, S. Siol, D. O. Scanlon, A. Zakutayev, A. Walsh, I. C. Smith, B. C. Melot, R. C. Kurchin, Y. Wang, J. Shi, F. C. Marques, J. J. Berry, W. Tumas, S. Lany, V. Stevanović, M. F. Toney, T. Buonassisi, *Chem. Mater.* **2017**, *29*, 1964.
[61] W. Liu, J. Zheng, M. Shang, Z. Fang, K.-C. Chou, W. Yang, X. Hou, T. Wu, *J. Mater. Chem. A* **2019**, *7*, 10912.
[62] W. Kong, Z. Ye, Z. Qi, B. Zhang, M. Wang, A. Rahimi-Iman, H. Wu, *Phys. Chem. Chem. Phys.* **2015**, *17*, 16405.
[63] Q. Han, S. H. Bae, P. Sun, Y. T. Hsieh, Y. Yang, Y. S. Rim, H. Zhao, Q. Chen, W. Shi, G. Li, Y. Yang, *Adv. Mater.* **2016**, *28*, 2253.
[64] V. M. Goldschmidt, *Naturwissenschaften* **1926**, *14*, 477.
[65] E. Smecca, Y. Numata, I. Deretzis, G. Pellegrino, S. Boninelli, T. Miyasaka, A. La Magna, A. Alberti, *Phys. Chem. Chem. Phys.* **2016**, *18*, 13413.
[66] W. Shockley, H. J. Queisser, *J. Appl. Phys.* **1961**, *32*, 510.
[67] T. Niu, J. Lu, M.-C. Tang, D. Barrit, D.-M. Smilgies, Z. Yang, J. Li, Y. Fan, T. Luo, I. McCulloch, A. Amassian, S. F. Liu, K. Zhao, *Energy Environ. Sci.* **2018**, *11*, 3358.
[68] J. W. Lee, Z. Dai, T. H. Han, C. Choi, S. Y. Chang, S. J. Lee, N. De Marco, H. Zhao, P. Sun, Y. Huang, Y. Yang, *Nat. Commun.* **2018**, *9*, 3021.
[69] J. W. Lee, D. J. Seol, A. N. Cho, N. G. Park, *Adv. Mater.* **2014**, *26*, 4991.
[70] J. W. Lee, Z. Dai, C. Lee, H. M. Lee, T. H. Han, N. De Marco, O. Lin, C. S. Choi, B. Dunn, J. Koh, D. Di Carlo, J. H. Ko, H. D. Maynard, Y. Yang, *J. Am. Chem. Soc.* **2018**, *140*, 6317.
[71] J. S. Yun, J. Kim, T. Young, R. J. Patterson, D. Kim, J. Seidel, S. Lim, M. A. Green, S. Huang, A. Ho-Baillie, *Adv. Funct. Mater.* **2018**, *28*, 1705363.
[72] S. Dastidar, C. J. Hawley, A. D. Dillon, A. D. Gutierrez-Perez, J. E. Spanier, A. T. Fafarman, *J. Phys. Chem. Lett.* **2017**, *8*, 1278.
[73] M. S. Kirschner, B. T. Diroll, P. Guo, S. M. Harvey, W. Helweh, N. C. Flanders, A. Brumberg, N. E. Watkins, A. A. Leonard, A. M. Evans, M. R. Wasielewski, W. R. Dichtel, X. Zhang, L. X. Chen, R. D. Schaller, *Nat. Commun.* **2019**, *10*, 504.
[74] H. Zhu, T. Cai, M. Que, J. P. Song, B. M. Rubenstein, Z. Wang, O. Chen, *J. Phys. Chem. Lett.* **2018**, *9*, 4199.
[75] S. Wozny, M. Yang, A. M. Nardes, C. C. Mercado, S. Ferrere, M. O. Reese, W. Zhou, K. Zhu, *Chem. Mater.* **2015**, *27*, 4814.
[76] P. Postorino, L. Malavasi, *J. Phys. Chem. Lett.* **2017**, *8*, 2613.
[77] I. Deretzis, A. Alberti, G. Pellegrino, E. Smecca, F. Giannazzo, N. Sakai, T. Miyasaka, A. La Magna, *Appl. Phys. Lett.* **2015**, *106*, 131904.
[78] L. Malavasi, C. A. Fisher, M. S. Islam, *Chem. Soc. Rev.* **2010**, *39*, 4370.
[79] J. B. Goodenough, *Rep. Prog. Phys.* **2004**, *67*, 1915.
[80] R. L. Narayan, S. V. Suryanarayana, *Mater. Lett.* **1991**, *11*, 305.
[81] J. Mizusaki, K. Arai, K. Fueki, *Solid State Ionics* **1983**, *11*, 203.
[82] J. M. Azpiroz, E. Mosconi, J. Bisquert, F. De Angelis, *Energy Environ. Sci.* **2015**, *8*, 2118.
[83] Y. Shao, Z. Xiao, C. Bi, Y. Yuan, J. Huang, *Nat. Commun.* **2014**, *5*, 1.
[84] K. X. Steirer, P. Schulz, G. Teeter, V. Stevanovic, M. Yang, K. Zhu, J. J. Berry, *ACS Energy Lett.* **2016**, *1*, 360.
[85] C. Yi, J. Luo, S. Meloni, A. Boziki, N. Ashari-Astani, C. Grätzel, S. M. Zakeeruddin, U. Röthlisberger, M. Grätzel, *Energy Environ. Sci.* **2016**, *9*, 656.
[86] D. Chi, S. Huang, M. Zhang, S. Mu, Y. Zhao, Y. Chen, J. You, *Adv. Funct. Mater.* **2018**, *28*, 1804603.
[87] L. Q. Xie, L. Chen, Z. A. Nan, H. X. Lin, T. Wang, D. P. Zhan, J. W. Yan, B. W. Mao, Z. Q. Tian, *J. Am. Chem. Soc.* **2017**, *139*, 3320.

© 2020 WILEY-VCH Verlag GmbH & Co. KGaA, Weinheim

[88] Z. Li, M. Yang, J.-S. Park, S.-H. Wei, J. J. Berry, K. Zhu, *Chem. Mater.* **2016**, *28*, 284.
[89] M. Saliba, T. Matsui, K. Domanski, J. Y. Seo, A. Ummadisingu, S. M. Zakeeruddin, J. P. Correa-Baena, W. R. Tress, A. Abate, A. Hagfeldt, M. Gratzel, *Science* **2016**, *354*, 206.
[90] M. Saliba, T. Matsui, J. Y. Seo, K. Domanski, J. P. Correa-Baena, M. K. Nazeeruddin, S. M. Zakeeruddin, W. Tress, A. Abate, A. Hagfeldt, M. Gratzel, *Energy Environ. Sci.* **2016**, *9*, 1989.
[91] C. G. Bischak, C. L. Hetherington, H. Wu, S. Aloni, D. F. Ogletree, D. T. Limmer, N. S. Ginsberg, *Nano Lett.* **2017**, *17*, 1028.
[92] S. Draguta, O. Sharia, S. J. Yoon, M. C. Brennan, Y. V. Morozov, J. S. Manser, P. V. Kamat, W. F. Schneider, M. Kuno, *Nat. Commun.* **2017**, *8*, 200.
[93] D. J. Kubicki, D. Prochowicz, A. Hofstetter, S. M. Zakeeruddin, M. Grätzel, L. Emsley, *J. Am. Chem. Soc.* **2017**, *139*, 14173.
[94] M. C. Brennan, S. Draguta, P. V. Kamat, M. Kuno, *ACS Energy Lett.* **2017**, *3*, 204.
[95] R. F. Egerton, P. Li, M. Malac, *Micron* **2004**, *35*, 399.
[96] R. F. Egerton, *Ultramicroscopy* **2013**, *127*, 100.
[97] L. A. Baker, J. L. Rubinstein, *Methods in Enzymology*, Vol. *481*, Elsevier, Amsterdam **2010**, p. 371.
[98] D. Zhang, Y. Zhu, L. Liu, X. Ying, C. E. Hsiung, R. Sougrat, K. Li, Y. Han, *Science* **2018**, *359*, 675.
[99] M. Adrian, J. Dubochet, J. Lepault, A. W. McDowall, *Nature* **1984**, *308*, 32.
[100] E. Knapek, J. Dubochet, *J. Mol. Biol.* **1980**, *141*, 147.
[101] A. Lu, V. G. Magupalli, J. Ruan, Q. Yin, M. K. Atianand, M. R. Vos, G. F. Schroder, K. A. Fitzgerald, H. Wu, E. H. Egelman, *Cell* **2014**, *156*, 1193.
[102] X. Wang, Y. Li, Y. S. Meng, *Joule* **2018**, *2*, 2225.
[103] M. Ballauff, Y. Lu, *Polymer* **2007**, *48*, 1815.
[104] Y. Li, W. Zhou, Y. Li, W. Huang, Z. Zhang, G. Chen, H. Wang, G.-H. Wu, N. Rolston, R. Vila, W. Chiu, Y. Cui, *Joule* **2019**, *3*, 2854.
[105] X. Wang, M. Zhang, J. Alvarado, S. Wang, M. Sina, B. Lu, J. Bouwer, W. Xu, J. Xiao, J. G. Zhang, J. Liu, Y. S. Meng, *Nano Lett.* **2017**, *17*, 7606.
[106] R. F. Thompson, M. Walker, C. A. Siebert, S. P. Muench, N. A. Ranson, *Methods* **2016**, *100*, 3.
[107] M. Gao, Y. K. Kim, C. Zhang, V. Borshch, S. Zhou, H. S. Park, A. Jákli, O. D. Lavrentovich, M. G. Tamba, A. Kohlmeier, G. H. Mehl, W. Weissflog, D. Studer, B. Zuber, H. Gnägi, F. Lin, *Micros. Res. Tech.* **2014**, *77*, 754.
[108] J. Mayer, L. A. Giannuzzi, T. Kamino, J. Michael, *MRS Bull.* **2007**, *32*, 400.
[109] A. Rigort, J. M. Plitzko, *Arch. Biochem. Biophys.* **2015**, *581*, 122.
[110] W. Chiu, *Annu. Rev. Biophys. Biophys. Chem.* **1986**, *15*, 237.
[111] P. S. Whitfield, N. Herron, W. E. Guise, K. Page, Y. Q. Cheng, I. Milas, M. K. Crawford, *Sci. Rep.* **2016**, *6*, 35685.
[112] H. Hosokawa, R. Tamaki, T. Sawada, A. Okonogi, H. Sato, Y. Ogomi, S. Hayase, Y. Okada, T. Yano, *Nat. Commun.* **2019**, *10*, 43.
[113] B. Chen, Z. J. Yu, S. Manzoor, S. Wang, W. Weigand, Z. Yu, G. Yang, Z. Ni, X. Dai, Z. C. Holman, J. Huang, *Joule* **2020**, *4*, 850.
[114] S. Chen, Y. Zhang, J. Zhao, Z. Mi, J. Zhang, J. Cao, J. Feng, G. Zhang, J. Qi, J. Li, P. Gao, *Sci. Bull.* **2020**, In press, https://doi.org/10.1016/j.scib.2020.05.020.
[115] O. Hentz, Z. Zhao, S. Gradecak, *Nano Lett.* **2016**, *16*, 1485.
[116] M. U. Rothmann, W. Li, Y. Zhu, A. Liu, Z. Ku, U. Bach, J. Etheridge, Y. B. Cheng, *Adv. Mater.* **2018**, *30*, 1800629.
[117] N. A. Rivas, A. Babayigit, B. Conings, T. Schwarz, A. Sturm, A. Garzon Manjon, O. Cojocaru-Miredin, B. Gault, F. U. Renner, *PLoS One* **2020**, *15*, e0227920.
[118] Y. C. Zhao, W. K. Zhou, X. Zhou, K. H. Liu, D. P. Yu, Q. Zhao, *Light Sci. Appl.* **2017**, *6*, e16243.
[119] F. Babbe, C. M. Sutter-Fella, *Adv. Energy Mater.* **2020**, 1903587.
[120] M. Kodur, R. E. Kumar, Y. Luo, D. N. Cakan, X. Li, M. Stuckelberger, D. P. Fenning, *Adv. Energy Mater.* **2020**, 1903170.
[121] L. E. Mundt, L. T. Schelhas, *Adv. Energy Mater.* **2019**, 1903074.
[122] Z. Song, S. C. Watthage, A. B. Phillips, M. J. Heben, *J. Photonics Energy* **2016**, *6*, 022001.
[123] W.-J. Yin, J.-H. Yang, J. Kang, Y. Yan, S.-H. Wei, *J. Mater. Chem. A* **2015**, *3*, 8926.
[124] Y. Li, L. Ji, R. Liu, C. Zhang, C. H. Mak, X. Zou, H.-H. Shen, S.-Y. Leu, H.-Y. Hsu, *J. Mater. Chem. A* **2018**, *6*, 12842.
[125] M. V. Kovalenko, L. Protesescu, M. I. Bodnarchuk, *Science* **2017**, *358*, 745.
[126] G. Lee, M.-c. Kim, Y. W. Choi, N. Ahn, J. Jang, J. Yoon, S. M. Kim, J.-G. Lee, D. Kang, H. S. Jung, M. Choi, *Energy Environ. Sci.* **2019**, *12*, 3182.
[127] D. Bi, X. Li, J. V. Milic, D. J. Kubicki, N. Pellet, J. Luo, T. LaGrange, P. Mettraux, L. Emsley, S. M. Zakeeruddin, M. Gratzel, *Nat. Commun.* **2018**, *9*, 4482.
[128] G. Divitini, S. Cacovich, F. Matteocci, L. Cinà, A. Di Carlo, C. Ducati, *Nat. Energy* **2016**, *1*, 1.
[129] B. Yang, O. Dyck, W. Ming, M. H. Du, S. Das, C. M. Rouleau, G. Duscher, D. B. Geohegan, K. Xiao, *ACS Appl. Mater. Interfaces* **2016**, *8*, 32333.
[130] T. W. Kim, N. Shibayama, L. Cojocaru, S. Uchida, T. Kondo, H. Segawa, *Adv. Funct. Mater.* **2018**, *28*, 1804039.
[131] Z. Fan, H. Xiao, Y. Wang, Z. Zhao, Z. Lin, H.-C. Cheng, S.-J. Lee, G. Wang, Z. Feng, W. A. Goddard Iii, Y. Huang, X. Duan, *Joule* **2017**, *1*, 548.
[132] Q. Jeangros, M. Duchamp, J. Werner, M. Kruth, R. E. Dunin-Borkowski, B. Niesen, C. Ballif, A. Hessler-Wyser, *Nano Lett.* **2016**, *16*, 7013.
[133] H. J. Jung, D. Kim, S. Kim, J. Park, V. P. Dravid, B. Shin, *Adv. Mater.* **2018**, *30*, e1802769.
[134] G. Love, V. D. Scott, N. M. T. Dennis, L. Laurenson, *Scanning* **1981**, *4*, 32.
[135] L. M. Herz, *Annu. Rev. Phys. Chem.* **2016**, *67*, 65.
[136] G. Xing, B. Wu, X. Wu, M. Li, B. Du, Q. Wei, J. Guo, E. K. Yeow, T. C. Sum, W. Huang, *Nat. Commun.* **2017**, *8*, 14558.
[137] J. Peng, Y. Chen, K. Zheng, T. Pullerits, Z. Liang, *Chem. Soc. Rev.* **2017**, *46*, 5714.
[138] C. Li, A. Guerrero, S. Huettner, J. Bisquert, *Nat. Commun.* **2018**, *9*, 5113.
[139] X. Deng, X. Wen, J. Zheng, T. Young, C. F. J. Lau, J. Kim, M. Green, S. Huang, A. Ho-Baillie, *Nano Energy* **2018**, *46*, 356.
[140] J. Y. Ma, J. Ding, H. J. Yan, D. Wang, J. S. Hu, *ACS Appl. Mater. Interfaces* **2019**, *11*, 21627.
[141] J. J. van Franeker, K. H. Hendriks, B. J. Bruijnaers, M. W. G. M. Verhoeven, M. M. Wienk, R. A. J. Janssen, *Adv. Energy Mater.* **2017**, *7*, 1601822.
[142] H. Hu, Z. Ren, P. W. K. Fong, M. Qin, D. Liu, D. Lei, X. Lu, G. Li, *Adv. Funct. Mater.* **2019**, *29*, 1900092.
[143] Y. Zhao, H. Tan, H. Yuan, Z. Yang, J. Z. Fan, J. Kim, O. Voznyy, X. Gong, L. N. Quan, C. S. Tan, J. Hofkens, D. Yu, Q. Zhao, E. H. Sargent, *Nat. Commun.* **2018**, *9*, 1607.
[144] E. Lifshin, *X-Ray Characterization of Materials*, Wiley, New York **2008**.
[145] S. R. Stock, *In situ X-ray Measurement Methods. In Characterization of Materials* (Ed: E. N. Kaufmann), **2012**, https://doi.org/10.1002/0471266965.com134.
[146] M. Morcrette, Y. Chabre, G. Vaughan, G. Amatucci, J. B. Leriche, S. Patoux, C. Masquelier, J. M. Tarascon, *Electrochim. Acta* **2002**, *47*, 3137.
[147] Y. Gorlin, B. Lassalle-Kaiser, J. D. Benck, S. Gul, S. M. Webb, V. K. Yachandra, J. Yano, T. F. Jaramillo, *J. Am. Chem. Soc.* **2013**, *135*, 8525.
[148] L. S. Dubrovinsky, S. K. Saxena, F. Tutti, S. Rekhi, T. LeBehan, *Phys. Rev. Lett.* **2000**, *84*, 1720.

© 2020 WILEY-VCH Verlag GmbH & Co. KGaA, Weinheim

[149] J. S. Yoo, G. S. Han, S. Lee, M. C. Kim, M. Choi, H. S. Jung, J.-K. Lee, *Nano Res.* **2017**, *10*, 3885.
[150] D. G. Lee, M. C. Kim, S. Wang, B. J. Kim, Y. S. Meng, H. S. Jung, *ACS Appl. Mater Interfaces* **2019**, *11*, 48497.
[151] S. R. Raga, M.-C. Jung, M. V. Lee, M. R. Leyden, Y. Kato, Y. Qi, *Chem. Mater.* **2015**, *27*, 1597.
[152] P. Pistor, J. Borchert, W. Franzel, R. Csuk, R. Scheer, *J. Phys. Chem. Lett.* **2014**, *5*, 3308.
[153] X. Song, W. Wang, P. Sun, W. Ma, Z.-K. Chen, *Appl. Phys. Lett.* **2015**, *106*, 033901.
[154] M. Alsari, O. Bikondoa, J. Bishop, M. Abdi-Jalebi, L. Y. Ozer, M. Hampton, P. Thompson, M. T. Hörantner, S. Mahesh, C. Greenland, J. E. Macdonald, G. Palmisano, H. J. Snaith, D. G. Lidzey, S. D. Stranks, R. H. Frienda, S. Lilliu, *Energy Environ. Sci.* **2018**, *11*, 383.
[155] J. A. Aguiar, S. Wozny, T. G. Holesinger, T. Aoki, M. K. Patel, M. Yang, J. J. Berry, M. Al-Jassim, W. Zhou, K. Zhu, *Energy Environ. Sci.* **2016**, *9*, 2372.
[156] K. H. Stone, A. Gold-Parker, V. L. Pool, E. L. Unger, A. R. Bowring, M. D. McGehee, M. F. Toney, C. J. Tassone, *Nat. Commun.* **2018**, *9*, 1.
[157] Y. Zhong, R. Munir, J. Li, M.-C. Tang, M. R. Niazi, D.-M. Smilgies, K. Zhao, A. Amassian, *ACS Energy Lett.* **2018**, *3*, 1078.
[158] M. Qin, K. Tse, T. K. Lau, Y. Li, C. J. Su, G. Yang, J. Chen, J. Zhu, U. S. Jeng, G. Li, H. Chen, X. Lu, *Adv. Mater.* **2019**, *31*, e1901284.
[159] H. Tsai, R. Asadpour, J. C. Blancon, C. C. Stoumpos, O. Durand, J. W. Strzalka, B. Chen, R. Verduzco, P. M. Ajayan, S. Tretiak, J. Even, M. A. Alam, M. G. Kanatzidis, W. Nie, A. D. Mohite, *Science* **2018**, *360*, 67.
[160] T. Niu, J. Lu, R. Munir, J. Li, D. Barrit, X. Zhang, H. Hu, Z. Yang, A. Amassian, K. Zhao, S. F. Liu, *Adv. Mater.* **2018**, *30*, e1706576.
[161] C. Das, M. Wussler, T. Hellmann, T. Mayer, W. Jaegermann, *Phys. Chem. Chem. Phys.* **2018**, *20*, 17180.
[162] J. C.-R. Ke, A. S. Walton, D. J. Lewis, A. Tedstone, P. O'Brien, A. G. Thomas, W. R. Flavell, *Chem. Commun.* **2017**, *53*, 5231.
[163] B.-A. Chen, J.-T. Lin, N.-T. Suen, C.-W. Tsao, T.-C. Chu, Y.-Y. Hsu, T.-S. Chan, Y.-T. Chan, J.-S. Yang, C.-W. Chiu, H. M. Chen, *ACS Energy Lett.* **2017**, *2*, 342.
[164] J.-W. Lee, S.-G. Kim, J.-M. Yang, Y. Yang, N.-G. Park, *APL Mater.* **2019**, *7*, 041111.
[165] Y. Shao, Y. Fang, T. Li, Q. Wang, Q. Dong, Y. Deng, Y. Yuan, H. Wei, M. Wang, A. Gruverman, J. Shield, J. Huang, *Energy Environ. Sci.* **2016**, *9*, 1752.
[166] T. A. Berhe, W.-N. Su, C.-H. Chen, C.-J. Pan, J.-H. Cheng, H.-M. Chen, M.-C. Tsai, L.-Y. Chen, A. A. Dubale, B.-J. Hwang, *Energy Environ. Sci.* **2016**, *9*, 323.
[167] Y. Han, S. Meyer, Y. Dkhissi, K. Weber, J. M. Pringle, U. Bach, L. Spiccia, Y.-B. Cheng, *J. Mater. Chem. A* **2015**, *3*, 8139.
[168] R. Wang, M. Mujahid, Y. Duan, Z. K. Wang, J. Xue, Y. Yang, *Adv. Funct. Mater.* **2019**, *29*, 1808843.
[169] S. Cacovich, G. Divitini, C. Ireland, F. Matteocci, A. Di Carlo, C. Ducati, *ChemSusChem* **2016**, *9*, 2673.
[170] D. Xu, X. Hua, S. C. Liu, H. W. Qiao, H. G. Yang, Y. T. Long, H. Tian, *Chem. Commun.* **2018**, *54*, 5434.
[171] J. Hidalgo, A. F. Castro-Méndez, J. P. Correa-Baena, *Adv. Energy Mater.* **2019**, *9*, 1900444.
[172] Y. Kanemitsu, *J. Mater. Chem. C* **2017**, *5*, 3427.
[173] S. Ghosh, Y. Bhandari, M. Groeber, *Comput.-Aided Des.* **2008**, *40*, 293.
[174] J. Zhang, A. A. Polycarpou, J. Economy, *Tribol. Lett.* **2010**, *38*, 355.
[175] D. W. deQuilettes, S. M. Vorpahl, S. D. Stranks, H. Nagaoka, G. E. Eperon, M. E. Ziffer, H. J. Snaith, D. S. Ginger, *Science* **2015**, *348*, 683.
[176] E. M. Tennyson, B. Roose, J. L. Garrett, C. Gong, J. N. Munday, A. Abate, M. S. Leite, *ACS Nano* **2019**, *13*, 1538.
[177] V. W. Bergmann, S. A. Weber, F. Javier Ramos, M. K. Nazeeruddin, M. Gratzel, D. Li, A. L. Domanski, I. Lieberwirth, S. Ahmad, R. Berger, *Nat. Commun.* **2014**, *5*, 5001.
[178] Y. Kutes, Y. Zhou, J. L. Bosse, J. Steffes, N. P. Padture, B. D. Huey, *Nano Lett.* **2016**, *16*, 3434.
[179] Y. Luo, P. Khoram, S. Brittman, Z. Zhu, B. Lai, S. P. Ong, E. C. Garnett, D. P. Fenning, *Adv. Mater.* **2017**, *29*, 1703451.
[180] J. P. Correa-Baena, Y. Luo, T. M. Brenner, J. Snaider, S. Sun, X. Li, M. A. Jensen, N. T. P. Hartono, L. Nienhaus, S. Wieghold, J. R. Poindexter, S. Wang, Y. S. Meng, T. Wang, B. Lai, M. V. Holt, Z. Cai, M. G. Bawendi, L. Huang, T. Buonassisi, D. P. Fenning, *Science* **2019**, *363*, 627.
[181] R. Szostak, J. C. Silva, S. H. Turren-Cruz, M. M. Soares, R. O. Freitas, A. Hagfeldt, H. C. N. Tolentino, A. F. Nogueira, *Sci. Adv.* **2019**, *5*, eaaw6619.
[182] K. Domanski, J. P. Correa-Baena, N. Mine, M. K. Nazeeruddin, A. Abate, M. Saliba, W. Tress, A. Hagfeldt, M. Gratzel, *ACS Nano* **2016**, *10*, 6306.
[183] W.-C. Lin, H.-Y. Chang, K. Abbasi, J.-J. Shyue, C. Burda, *Adv. Mater. Interfaces* **2017**, *4*, 1600673.
[184] S. Wang, M. Sina, P. Parikh, T. Uekert, B. Shahbazian, A. Devaraj, Y. S. Meng, *Nano Lett.* **2016**, *16*, 5594.
[185] J. F. Galisteo-Lopez, Y. Li, H. Miguez, *J. Phys. Chem. Lett.* **2016**, *7*, 5227.
[186] S. Wang, A. Cabreros, Y. Yang, A. S. Hall, S. Valenzuela, Y. Luo, J. Correa-Baena, M.-c. Kim, O. Fjeldberg, D. P. Fenning, Y. S. Meng, *Cell Rep. Phys. Sci.* **2020**, https://doi.org/10.1016/j.xcrp.2020.100103.
[187] T. A. S. Doherty, A. J. Winchester, S. Macpherson, D. N. Johnstone, V. Pareek, E. M. Tennyson, S. Kosar, F. U. Kosasih, M. Anaya, M. Abdi-Jalebi, Z. Andaji-Garmaroudi, E. L. Wong, J. Madeo, Y. H. Chiang, J. S. Park, Y. K. Jung, C. E. Petoukhoff, G. Divitini, M. K. L. Man, C. Ducati, A. Walsh, P. A. Midgley, K. M. Dani, S. D. Stranks, *Nature* **2020**, *580*, 360.
[188] Z. Ni, C. Bao, Y. Liu, Q. Jiang, W.-Q. Wu, S. Chen, X. Dai, B. Chen, B. Hartweg, Z. Yu, Z. Holman, J. Huang, *Science* **2020**, *367*, 1352.
[189] J. Liu, J. Leng, S. Wang, J. Zhang, S. Jin, *J. Phys. Chem. Lett.* **2019**, *10*, 97.
[190] Y. Zhou, H. F. Garces, N. P. Padture, *Front. Optoelectron.* **2016**, *9*, 81.
[191] Y. Tian, I. G. Scheblykin, *J. Phys. Chem. Lett.* **2015**, *6*, 3466.
[192] M. S. Alias, Y. Yang, T. K. Ng, I. Dursun, D. Shi, M. I. Saidaminov, D. Priante, O. M. Bakr, B. S. Ooi, *J. Phys. Chem. Lett.* **2016**, *7*, 137.
[193] Z. Li, C. Xiao, Y. Yang, S. P. Harvey, D. H. Kim, J. A. Christians, M. Yang, P. Schulz, S. U. Nanayakkara, C.-S. Jiang, J. M. Luther, J. J. Berry, M. C. Beard, M. M. Al-Jassima, K. Zhu, *Energy Environ. Sci.* **2017**, *10*, 1234.
[194] S. P. Harvey, F. Zhang, A. Palmstrom, J. M. Luther, K. Zhu, J. J. Berry, *ACS Appl. Mater. Interfaces* **2019**, *11*, 30911.
[195] H. Yuan, E. Debroye, K. Janssen, H. Naiki, C. Steuwe, G. Lu, M. l. Moris, E. Orgiu, H. Uji-i, F. De Schryver, P. Samorì, J. Hofkens, M. Roeffaers, *J. Phys. Chem. Lett.* **2016**, *7*, 561.
[196] A. R. Milosavljević, W. Huang, S. Sadhu, S. Ptasinska, *Angew. Chem., Int. Ed.* **2016**, *55*, 10083.
[197] Z. Dang, J. Shamsi, F. Palazon, M. Imran, Q. A. Akkerman, S. Park, G. Bertoni, M. Prato, R. Brescia, L. Manna, *ACS Nano* **2017**, *11*, 2124.
[198] S. Bae, S. Kim, S. W. Lee, K. J. Cho, S. Park, S. Lee, Y. Kang, H. S. Lee, D. Kim, *J. Phys. Chem. Lett.* **2016**, *7*, 3091.
[199] Y. Rakita, I. Lubomirsky, D. Cahen, *Mater. Horiz.* **2019**, *6*, 1297.
[200] Y. H. Park, I. Jeong, S. Bae, H. J. Son, P. Lee, J. Lee, C. H. Lee, M. J. Ko, *Adv. Funct. Mater.* **2017**, *27*, 1605988.
[201] Y. Yuan, T. Li, Q. Wang, J. Xing, A. Gruverman, J. Huang, *Sci. Adv.* **2017**, *3*, e1602164.

© 2020 WILEY-VCH Verlag GmbH & Co. KGaA, Weinheim

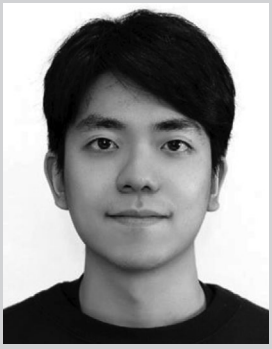

Min-cheol Kim is a Postdoctoral Researcher in Prof. Shirley Meng's group in University of California San Diego (UCSD) from 2019. He received a B.S. and Ph.D. in Department of Mechanical Engineering from Seoul National University (SNU), Korea, in 2012 and 2018, respectively. His research has been focused on the development of perovskite photovoltaics by investigating degradation mechanisms and demonstrating highly efficient and flexible perovskite solar cells.

Ying Shirley Meng is the Zable Endowed Chair Professor in Energy Technologies and the Director of Sustinable Power & Energy Center (SPEC) at University of California San Diego (UCSD). Her research group—Laboratory for Energy Storage and Conversion (LESC)—focuses on functional nano- and microscale materials for energy storage and conversion.

© 2020 WILEY-VCH Verlag GmbH & Co. KGaA, Weinheim